

Development of Al-Based Nanocomposites Using CNT-GnP-hBN Ternary Hybrid Reinforcement

Arka Ghosh^a, Sourav Ganguly^b, Nasimul Alam Syed^{a*} 

^aNational Institute of Technology Rourkela, Department of Metallurgical and Materials Engineering, 769008, Rourkela, India.

^bCSIR-Institute of Minerals and Materials Technology (IMMT), Department of Advanced Materials Technology, 751003, Bhubaneswar, India.

Received: May 26, 2023; Revised: July 18, 2023; Accepted: July 29, 2023

Aluminium (Al) has low strength, limiting its applicability for certain technical applications seeking higher mechanical strength and deformation resistance. Integration of ternary hybrid reinforcement in Al offers a compelling opportunity to achieve a synergistic combination of multiple desirable properties opening new avenues for advanced engineering applications beyond what can be achieved with mono or binary reinforcement systems. Here, Al-based nanocomposites were developed by incorporating a ternary hybrid reinforcement system, consisting of graphite nanoplatelets (GnP), hBN and MWCNT. Al-1 wt.% GnP_{0.3}CNT_{0.3}hBN_{0.4}, Al-2 wt.% GnP_{0.3}CNT_{0.3}hBN_{1.4}, Al-3 wt.% GnP_{0.3}CNT_{0.3}hBN_{2.4}, and Al-5 wt.% GnP_{0.3}CNT_{0.3}hBN_{4.4} nanocomposites were developed by powder metallurgy (PM) route. The results indicate that the Al-1 wt.% GnP_{0.3}MWCNT_{0.3}hBN_{0.4} hybrid nanocomposite exhibits the highest wear resistance. Among the hBN-based nanocomposites, Al-3 wt.% hBN nanocomposite exhibited the best wear properties. Increasing the hBN loading level in the CNT-GnP-hBN ternary nanofiller system beyond 0.4 wt.% resulted in a deterioration of physical, mechanical and wear properties. Al-1 wt.% CNT_{0.3}GnP_{0.3}hBN_{0.4} hybrid nanocomposite had the highest relative density and hardness of ~92.56% of ~415.91 MPa respectively. The compressive strength (σ_{\max}) of Al-1 wt.% CNT_{0.3}GnP_{0.3}hBN_{0.4} hybrid nanocomposite was ~874.77 MPa, while the σ_{\max} rapidly declined in the nanocomposites with the increased content of the CNT-GnP-hBN hybrid nanofiller.

Keywords: Al-based nanocomposites, powder metallurgy (PM), hexagonal boron nitride (hBN), graphite nanoplatelets (GnP), multiwalled carbon nanotubes (MWCNT), hardness, wear.

1. Introduction

Al and its alloys play a vital role in a wide range of industries like automotive and aerospace. Although Al and its alloys have extraordinary characteristics like high strength to weight ratio, toughness and fatigue resistance its mechanical properties like hardness, strength and wear resistance are still very low as compared to other metals and alloys. Nowadays automotive and aerospace industries need lightweight, strong and low-cost materials. The major objective for selecting such materials is to get better strength to weight ratio which consumes less energy. In order to achieve these properties hybrid composites, come to play. The hybrid composite contains two or more reinforcements with different shapes, sizes and properties which can provide better mechanical and tribological properties than single reinforcement composites. Al-matrix nanocomposites (AMnCs) refer to the category of high-performance lightweight Al-based material systems. For aerospace, automobile and industrial purpose SiC, B₄C, Al₂O₃, TiC have been widely used as reinforcement¹⁻³. In order to get a low-cost Al metal matrix with some extraordinary thermo-mechanical properties researchers have chosen to add hybrid nanoreinforcements in the Al matrix. In the 1D category generally, multiwalled or single-walled carbon nanotubes have been used, in the

2D category graphene and hexagonal boron nitride (hBN) have been used. The reason for using these materials as reinforcement is to offer high fracture toughness, high strength, high thermal conductivity, superior wear resistance and good fatigue resistance. For the last several years carbon-based reinforcements having 1D and 2D structures have fascinated researchers. In the 1D category, single walled carbon nanotubes (SWCNT) and multiwalled carbon nanotubes (MWCNT) make an immense effect as reinforcement because of their extraordinary mechanical and physical properties. The Young's modulus of MWCNT lies in the range of ~1.7-2.4 TPa and its theoretical specific surface area lies in the range of ~400-70 m²/g. The thermal conductivity of MWCNTs is ~2586 W/mK^{4,5} and their electrical conductivity is 49.49 S/cm. In recent years 2D atomic-level thickness crystal materials like graphene and hBN have attracted widespread interest. Both these 2D materials have a lot of excellent characteristics such as high specific area and high Young's modulus. 2D hBN has gained tremendous attention due to its profound mechanical strength, remarkable oxidation resistance and unique atom-thick structure. hBN is a layered material with a honeycomb structure analogous to that of graphene. Within each layer, it is composed of alternating B and N atoms that are arranged in sp² bonded network. The bond length

*e-mail: nasimulalam@yahoo.com

between B and N atoms in hBN is 1.44 Å, whereas the bond length between C atoms in graphene is 1.42 Å. hBN has a lattice constant of 2.50 Å which is very similar to that of graphene (2.46 Å). Within each hBN layer the atoms of B and N are held together by strong covalent bonds, while the layers are held together by relatively weak van der Waals forces and the interplanar distance is 3.33 Å as shown in Figure 1⁶. Monolayer graphene and hBN a lattice mismatch of only about 1.5%. hBN is an insulating 2D material with a large bandgap (~6.08 eV). The elastic modulus of hBN was evaluated to be 0.8 TPa and its tensile strength was found to be 100 GPa which is comparable to that of graphene. In recent years, hBN has been widely used in many fields such as electronic devices, pollutant adsorption, composite materials and lubricity^{7,8}. Graphene has a very stable honeycomb structure and the length of the C-C bond is 1.42 Å and the interplanar distance between two layers is 3.35 Å. The C atoms are sp^2 hybridized and a single C atom is surrounded by three neighbouring C atoms which are bonded by a strong σ bond. Graphene is the thinnest and hardest material ever produced by scientists. It has a tensile strength of 125 GPa and elastic modulus of 1.1 TPa and a 2D ultimate plane strength of 42 N/m². It has a thermal conductivity of 5.5×10^3 W/m.^{°K} and carrier mobility of 2×10^5 cm²/V.s⁹⁻¹¹. The specific surface area of graphene is 2630 m²/g. Due to these extraordinary properties graphene has been widely used as thermal conductivity materials, energy storage materials, construction materials, and for developing nanoelectronic devices. Due to their superior mechanical properties both graphene and hBN are highly suitable for use as a nanofillers in nanocomposites¹²⁻¹⁴.

One the major drawbacks of Al and its alloys is its poor tribological characteristics, high coefficient of thermal expansion, low elastic modulus and strength. To enhance these properties different nanofillers have been incorporated into Al and its alloys¹⁵⁻¹⁸. Research in the area of nanocomposites is evolving towards using combinations of different nanofillers in order to achieve superior properties in the nanocomposites¹⁹. Several researchers have focused on the use of ceramic material as a reinforcing agent due to its superior mechanical and tribological properties. The impact of sintering processes (conventional, CS, and electric resistance, ERS) and SiC content (1, 3, and 5 wt.%) on the microstructural, mechanical, and tribological properties of Al-SiC composites were investigated by Shaikh et al.²⁰. According to the data, using SiC enhanced the hardness, wear resistance, and coefficient of friction (COF).

In particular, the addition of 5% SiC improved CS sintering hardness by 32% and ERS sintering hardness by 30%. Similarly, wear resistance improved by 37% for CS and 40% for ERS, while COF improved by 3% for CS (with 3 wt.% SiC) and 6% for ERS (with 5 wt.% SiC) compared to pure Al. Furthermore, ERS-processed composites showed enhanced densification, hardness (12-14%), and tribological behaviour, with wear resistance improvements of 36-39% and COF increases of 7-15% for SiC content ranging from 1 to 5 wt.%. Wear processes found in Al-SiC composites included abrasion, adhesion, and delamination, with ERS composites showing less adhesive wear. Liu et al.²¹ studied the effects of reduced graphene oxide (rGO) and graphene nanosheets (GNS) content on the characteristics of AMCs. At a maximum pressure of 560 MPa, the density achieved was 88.5% of the pore-free density, showing satisfactory compaction. The composites improved significantly in hardness, indicating the possibility of mass manufacture of components using this technology. However, more research is required to properly investigate the increases in strength and conductivity of these composites. The results showed that GNS reinforcement increased hardness more than rGO reinforcement, indicating that closeness to GNS boosted the reinforcing effect. For typical applications, graphene nanoparticle-reinforced AMCs have the potential to provide higher strength-to-weight ratios. However, there are still problems to overcome, such as producing effective and uniform dispersion, limiting undesired oxide formation during powder metallurgy, and optimizing cold compaction pressures. Moreover, Shaikh et al.²² investigated the microstructural, mechanical, and tribological properties of Al-based composites reinforced with rice husk ash (RHA) at different weight percentages (5, 10, and 15% wt.%). The composites are made using powder metallurgy (PM), which allows for the use of RHA, an agricultural waste, while also increasing the mechanical and wear characteristics of the composites. The inclusion of RHA resulted in a 20% to 25% increase in hardness and a 15% to 40% increase in wear behaviour. Based on micrographic images of worn surfaces and wear detritus, the wear mechanism is explored. Furthermore, an artificial neural network (ANN) model is suggested to predict the wear behaviour of the composite, and the experimental findings are compared with the expected outcomes, indicating the efficacy of a well-trained ANN model in predicting tribological behaviour. Here, in the present work a hybrid nanofiller consisting of 1D MWCNT and 2D GnP and hBN producing a 3D CNT-GnP-hBN hybrid nanofiller has been used.

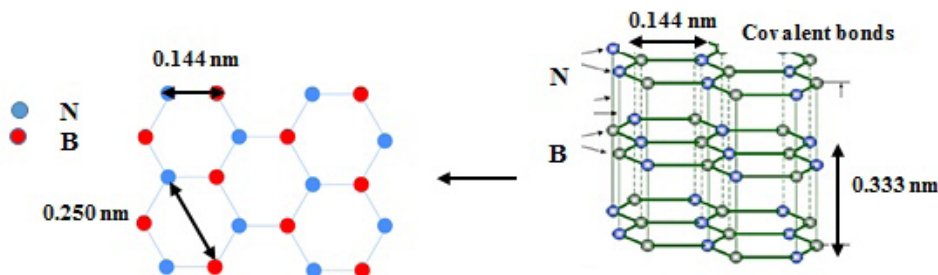


Figure 1. Structure of hBN⁶.

The effectiveness of the ternary hybrid nanofiller in improving the mechanical properties and wear behaviour of the Al-based nanocomposites has been investigated. The hybrid structure developed by blending the three nanofillers could not only provide the properties of the carbonaceous nanofillers, MWCNT and GnP, but also of hBN which has a structure similar to that of GnP. Although MWCNT, GnP and hBN are highly preferable nanoreinforcements in the Al matrix there are possibilities of formation of intermetallics between the Al matrix and the nanoreinforcements. These intermetallics are highly detrimental to the mechanical properties of the nanocomposites as they are very brittle. Aluminium carbide (Al_4C_3) can form at the interface of the Al matrix with the carbonaceous nanofillers like MWCNT and the GnP. Aluminium diboride (AlB_2) and aluminium nitride (AlN) can form by the reaction of the Al matrix with the B and N atoms respectively in the hBN. Figure 2 shows the binary phase diagrams of Al-C²³, Al-B²⁴ and Al-N²⁵ systems. Structural damage and defects in nanofillers can trigger interfacial reaction between the Al matrix and the nanofillers that lead to the formation of intermetallic phase²⁶.

The development of Al-based nanocomposites using a ternary hybrid reinforcement comprising of CNT, GnP and hBN to enhance the mechanical and wear properties of the nanocomposites is a novel area of research that has not been focused on previously. The innovative combination of these three different nanofillers each having unique properties can create a synergistic effect that can lead to significant improvement in the performance of the Al-based nanocomposites. The results of this research work can clearly show the effect of ternary hybrid nanofiller that is composed of 1D CNT and 2D GnP and hBN and the optimum composition of the ternary hybrid nanofiller and the manufacturing parameters in order to achieve the best properties in the nanocomposites. Al-based nanocomposites reinforced with ternary hybrid nanofiller comprising of CNT, GnP and hBN with varying weight fractions have been chosen to investigate the effect of these ternary hybrid nanofillers on the properties of the Al-based nanocomposites. This investigation helps to understand the role of hBN as a nanofiller when added in combination with carbonaceous nanofillers like CNT and GnP in enhancing the mechanical properties of the Al-based nanocomposites. The ternary hybrid reinforcement strategy aims to leverage the unique properties of each nanofiller, resulting in enhanced overall performance of the nanocomposites. Al-1 wt.% CNT_{0.3}GnP_{0.3}hBN_{0.4}, Al-2 wt.% CNT_{0.3}GnP_{0.3}hBN_{1.4}, Al-3 wt.% CNT_{0.3}GnP_{0.3}hBN_{2.4}, and Al-5 wt.% CNT_{0.3}GnP_{0.3}hBN_{4.4}

nanocomposites have been developed along with pure Al samples under similar conditions. The results can provide valuable insights into the optimal composition for achieving the desired mechanical, thermal, and tribological properties for specific applications.

Here, in the present study, Al-1 wt.% GnP_{0.3}CNT_{0.3}hBN_{0.4}, Al-2 wt.% GnP_{0.3}CNT_{0.3}hBN_{1.4}, Al-3 wt.% GnP_{0.3}CNT_{0.3}hBN_{2.4} and Al-5 wt.% GnP_{0.3}CNT_{0.3}hBN_{4.4} nanocomposites have been developed by powder metallurgy (PM) route. The morphology of the nanofillers as well as the microstructure of the sintered pure Al sample and the various Al-based nanocomposites was analysed using various analytical techniques. The relative density, hardness, tribological behaviour and compressive strength of the Al-based nanocomposites were determined and compared with the properties of the sintered pure Al sample developed similarly.

2. Experimental Details

Initially graphite nanoplatelets (GnP) were synthesized from natural flake graphite (NFG) by thermal exfoliation of the graphite intercalation compound (GIC). NFG was procured from Loba Chemie, India, having mesh size of 60 mesh and 98% purity. The GIC was synthesized by the intercalation of the NFG using concentrated sulphuric acid (H_2SO_4) along with hydrogen peroxide (H_2O_2). The GIC has been prepared at room temperature by mixing 6 g of NFG with 16 ml of concentrated H_2SO_4 (98%) and 1.5 ml of H_2O_2 (30%). The H_2SO_4 and the H_2O_2 were procured from Merck India. The GIC was obtained by 4 h of magnetic stirring of the foamy -Gr- H_2SO_4 -Gr- H_2SO_4 -Gr- compound. Later, the mixture was filtered 5-7 times with distilled water to remove the extra acids and achieve a GIC having a neutral pH followed by overnight heating of the precipitate in an oven at 80°C. In order to exfoliate it further and to obtain the thermally exfoliated graphite nanoplatelets (Th.ex.GnP) the GIC was then subjected to a thermal shock at 1000°C for 30 seconds in a muffle furnace to remove the intercalated acids. The Th.ex.GnP was further ultrasonicated for 20 h to get exfoliated graphite nanoplatelets (GnP). hBN having particle size of ~5 µm was procured from Oxford Lab Fine Chem LLP, India. In order to exfoliate the as-received hBN it was milled for 20 h. Acid-functionalized MWCNT having purity > 98% was procured from Platonic Nanotech, India. The CNT-GnP-hBN ternary hybrid nanofillers were synthesized by ultrasonicated MWCNT, GnP and hBN in proper weight fraction for 2 h in acetone medium. The ternary

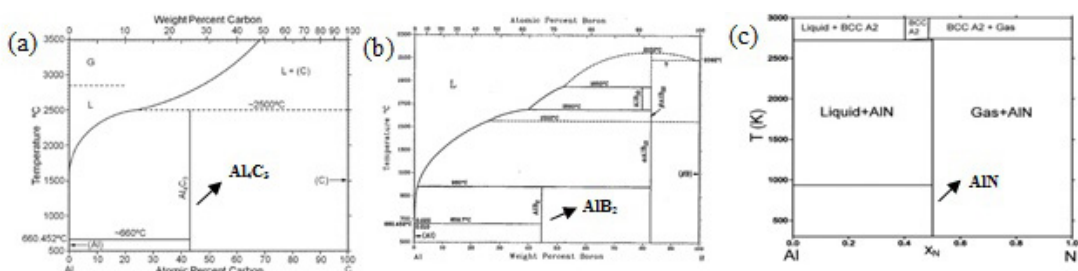


Figure 2. (a) Al-C, (b) Al-B and (c) Al-N binary phase diagrams.

hybrid nanofiller were later blended with the Al powder in proper weight fraction by ultrasonication. Ultrasonication of all samples was done for 2 h in acetone medium in the proportion 1:50, i.e. for 1 gm of the powder 50 ml acetone were taken. A high-intensity 1000 W ultrasonicator (Oscar Ultrasonics Pvt Ltd., model: Sonapros PR 1000 MP) equipped with a solid-state ultrasonic generator generating ultrasound in the frequency range of 2 ± 3 KHz and having a horn diameter of 12 mm was used. Acetone ($(\text{CH}_3)_2\text{CO}$) acts as a process cooling agent and it does not react with the solute particles and provides a uniform dispersion of the nanofiller. The various Al-CNT-GnP-hBN blended powders were compacted in a uniaxial compaction machine under a load of ~ 550 MPa for a holding time of 5 minutes to obtain green compacts having a diameter of 10 mm and thickness of 3-4 mm which were then sintered in a tubular furnace manufactured by Bysakh & Co, India at 550°C for 2 h in Ar atmosphere. The maximum attainable temperature of the furnace was 1700°C . Figure 3 shows the various steps involved in the development of the nanocomposites. Table 1 gives the composition of the various Al-CNT-GnP-hBN nanocomposites.

The various powder samples as well as the sintered samples were analysed by a D8 Bruker x-ray diffractometer using Co K_α radiation ($\lambda = 1.79026 \text{ \AA}$). The XRD analysis was done at $10^\circ/\text{minute}$ using a step size of 0.02 and in the 2θ range of $20\text{-}110^\circ$. The microstructural analysis of the

pure Al and the various Al-based nanocomposites were carried out using a Zeiss Axio Scope A1 optical microscope. A JEOL JSM-6480LV scanning electron microscope (SEM) and a ZEISS SUPRA 55 field emission electron microscope (FESEM) were used to analyze the surface morphology of the various powder samples as well as the microstructure of the sintered samples. The SEM was equipped with an energy dispersive x-ray spectroscope (EDXS) for the elemental analysis of the samples. The morphology of the various nanofiller powders were also analysed by using a FEI Tecnai F30 G2 S-TWIN high resolution transmission electron microscope (HRTEM) having a field emission gun (FEG). The operating voltage was 300 kV. The powder samples for HRTEM were made by sonicating them in acetone for five minutes and then applying a few drops with a glass pipette over a Cu grid with holes covered in carbon. Solid sintered samples were initially polished in a coarse emery paper till the thickness was below $100 \mu\text{m}$ for TEM sample preparation. Next, a disc punch is used to cut a 3-mm disc. Diamond paste is used to further polish this disc in a dimple grinder until the thickness is $20 \pm 5 \mu\text{m}$. The ground sample is then placed in an ion miller, where two ion guns alternately blast the sample with ions at 4 kV. The milling is halted, the samples are cleaned with acetone, and they are prepared for HRTEM analysis once a tiny hole has been made, ideally in the center of the sample. The density of the various sintered samples was determined using the Archimedes' principle.

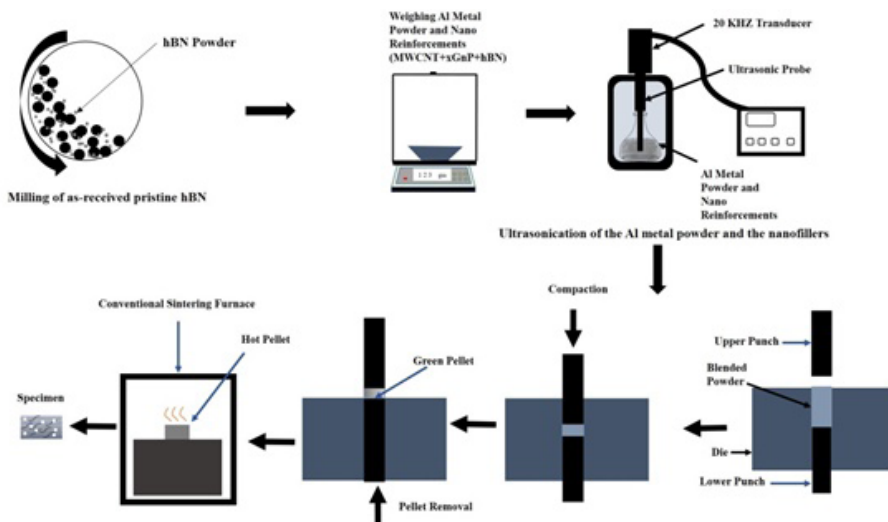


Figure 3. Schematic diagram showing the steps involved in the development of nanocomposites.

Table 1. Al-based hybrid nanocomposites.

Sample Name	Sample Composition			
	wt. % of Al	wt. % of CNT	wt. % of GnP	wt. % of hBN
$\text{A}_{99}\text{M}_{0.3}\text{G}_{0.3}\text{H}_{0.4}$	99	0.3	0.3	0.4
$\text{A}_{98}\text{M}_{0.3}\text{G}_{0.3}\text{H}_{1.4}$	98	0.3	0.3	1.4
$\text{A}_{97}\text{M}_{0.3}\text{G}_{0.3}\text{H}_{2.4}$	97	0.3	0.3	2.4
$\text{A}_{95}\text{M}_{0.3}\text{G}_{0.3}\text{H}_{4.4}$	95	0.3	0.3	4.4

A Contech (model - CB-300) density measuring kit was used to determine the density of the sintered samples. Three different weights, namely, dry weight (W_{dry}), dipped weight (W_{liquid}) and soaked weight (W_{soaked}) were measured to calculate the density of the samples. The samples were dipped in distilled water ($\rho = 1.0 \text{ gm/cc}$). The hardness of the polished sintered samples was determined using a Leco Micro Hardness Tester LM248AT. Vickers microhardness testing was done under a load of 10 gf for a dwell time of 10 seconds. The Raman spectra were acquired in the range of $500\text{-}3500 \text{ cm}^{-1}$ using a WITec Model-XMB3000 PL micro Raman spectrometer equipped with a WITec Alpha300 Confocal Raman microscope using an Ar⁺ polarized green laser having a wavelength of 532 nm was used. The Fourier transform infrared spectroscopy (FTIR) was recorded on a Bruker, Alpha E model spectrophotometer in the wavenumber range of $500\text{-}4000 \text{ cm}^{-1}$ using KBr as the mulling agent. The resolution of the infrared rays was maintained at 4 cm^{-1} . The sample scanning as well as background scanning was done 24 times. Differential Scanning Colorimetry (DSC) and thermogravimetric analysis (TGA) were carried out in a Netzsch STA 409C Simultaneous Thermal Analyzer (STA) in Ar atmosphere using Pt crucibles in the range of $25\text{-}1200^\circ\text{C}$ at a heating rate of $10^\circ\text{C}/\text{min}$. X-ray photoemission spectroscopy (XPS) was conducted using a PHI 5000 Versa Probe III Scanning XPS Microprobe. Al K α was used as the x-ray source which provided photons with 1486.6 eV energy. XPS photoemission spectra were taken using a pass energy of 55 eV. A ball-on-plate dry sliding wear tester (Ducom, India, model: TR 208 M1), the wear properties of the different sintered samples, including wear depth, wear loss, and wear rate, were determined. Keeping the ambient conditions constant (T 298 K, humidity of 40–60%), a hardened steel ball (SAE 52,100; 2 mm) was used to conduct the wear test and engrave wear tracks across the sintered samples at 15N load and at a speed of 20 rpm for 10 min. Compression tests were done to evaluate static compressive strength of the nanocomposites. The samples were prepared as per ASTM E9 standard for short specimen by maintaining a h/d ratio for the samples between 0.8 and 0.9. The compressive tests were carried out using Instrom 8862 universal testing machine (UTM) having a load capacity of upto 100 kN at a strain rate of 0.5 mm/min. The test was stopped when a crack was initiated in the sample. The obtained data was converted to σ - ϵ data and plotted to calculate the maximum compressive strength (σ_{max}) and strain to failure (ϵ_f).

3. Results and Discussion

Figure 4a shows the XRD spectra of the as-received natural flake graphite (NFG), the graphite intercalation compound (GIC), the thermally exfoliated graphite (Th. GIC) obtained after the GIC is given a thermal shock at 1000°C for 30 seconds and the GnP obtained by ultrasonication of the thermally exfoliated graphite for 20 h. Among the various peaks the most intense (002) peak was found at $2\theta = 30.95^\circ$ for the GnP sample and the interplanar spacing (d_{002}) determined using the Bragg's law ($\lambda = 2d_{002} \sin\theta$) was found to be 3.35 \AA ^{27,28}. However, by comparing the intensities of the (002) peaks in the XRD plots in Figure 4b it is evident that the intensity of the (002) peak is lowest in the case of GnP clearly indicating the lower number of graphene layers stacked together in the GnP which confirms the successful exfoliation of the NFG to obtain GnP. A slight shift in the (002) peak position in the XRD spectrum of GIC could be seen due to the attachment of the functional groups to the graphene layers during the synthesis of the GIC. Figure 5 shows the SEM images of the GnP that were used to synthesize the CNT-GnP-hBN ternary hybrid nanofiller which was later incorporated in the Al matrix as a reinforcement. The SEM images clearly indicate that the GnP have irregular and sharp edges and have a lateral dimension in the range of $\sim 0.15\text{-}0.4 \mu\text{m}$. Figure 6a-6d are the HRTEM images of the GnP and they clearly show that the GnP have a flaky morphology and have multiple layers of graphene stacked together. Few agglomerates of GnP and GnP having wrinkled edges as well as folding of the GnP edges could be seen. The HRTEM images in Figure 6b-6c show curved and corrugated edges of the GnP. The HRTEM images also indicate that the GnP are electron transparent and are found to be extremely stable under the exposure of the electron beam^{29,30}. The SAED pattern in Figure 6e shows sharp concentric diffraction rings along with bright spots clearly indicating the nanocrystalline nature of the GnP.

Figure 7a shows the Raman spectroscopy of GnP in range of $40\text{-}4000 \text{ cm}^{-1}$ obtained using an Ar⁺ polarized green laser having a wavelength of 532 nm. The G-band is the main spectral feature of graphene and appears at $\sim 1580 \text{ cm}^{-1}$ whereas the D-band can be seen at $\sim 1345 \text{ cm}^{-1}$. The G-band is a primary in-plane vibrational mode and the D-band, also known as the disorder band, occurs due to the lattice motion away from the middle of the Brillouin zone. The D-band can be used to characterize graphene-based materials with defects^{31,32}.

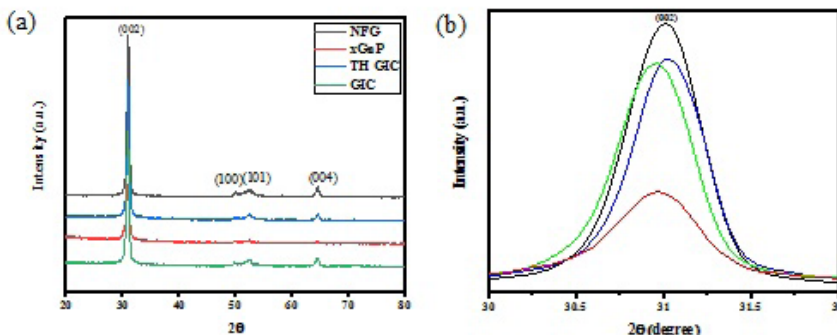


Figure 4. (a) XRD of NFG, GIC, thermally exfoliated graphite and GnP (b) (002) peak of of NFG, GIC, thermally exfoliated graphite and GnP.

The 2D-band at $\sim 2690\text{ cm}^{-1}$ is a second order overtone of a different in-plane vibration. FTIR analysis was done in order to determine the functional groups attached to the GnP. Figure 7b is the FTIR spectrum of the GnP. The broad peak at $\sim 3027\text{ cm}^{-1}$ is attributed to the stretching vibration of the hydroxyl (OH) bond and reveals the presence of OH groups in the GnP. The band observed at $\sim 1720\text{ cm}^{-1}$ can be assigned to the carboxyl (COOH) group. The absorption bands seen at ~ 2883 , ~ 2912 and $\sim 1192\text{ cm}^{-1}$ stem from the symmetric and asymmetric C-H stretching vibrations and C-H twisting. The peaks at ~ 1730 and $\sim 1630\text{ cm}^{-1}$ can be assigned to the stretching vibration of the carboxyl/carbonyl (C=O) and aromatic (C=C) groups respectively. It should be noted that the NFG was intercalated with concentrated H_2SO_4 for the synthesis of the GIC. The sharp peaks at ~ 1044 and $\sim 1226\text{ cm}^{-1}$ can be assigned to the ester (C-O) stretching vibrations. The FTIR spectrum shows a peak at $\sim 3425\text{ cm}^{-1}$ corresponding to the O-H stretching of the COOH group.

The broad peak occurring at $\sim 1450\text{ cm}^{-1}$ is due to the O-H deformations of C-OH groups³³.

The XPS spectrum of GnP in Figure 8a was done in order to obtain information about the type of bond in the GnP and is characterized by a highly intense band at 286.4 eV. Figure 8b shows the C 1s spectrum of the GnP. The XPS spectrum was fitted with Lorentzian-Gaussian peaks. The three peaks seen at 284.6 eV, 286.0 eV and 288.86 eV are attributed to the sp² carbon bonds, sp³ carbon bonds and carboxyl functional group (COOH) bonds respectively. Compositional analysis given along with the XPS spectrum in Figure 8a shows that the GnP consist of 92.3 at. % C, 4.5 at. % O and 2.8 at. % N. The presence of O could be due to the functional groups like COOH, C-O or C=O which were attached to the GnP during its synthesis or due to the oxidation of the GnP in air. Although the thermal shock was given to the GIC in Ar atmosphere at 1000°C for 30 seconds it could also be oxidized due to the presence of trace amount of oxygen as

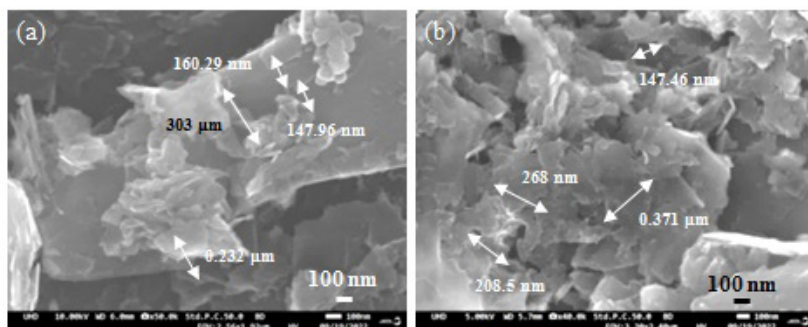


Figure 5. SEM images of GnP.

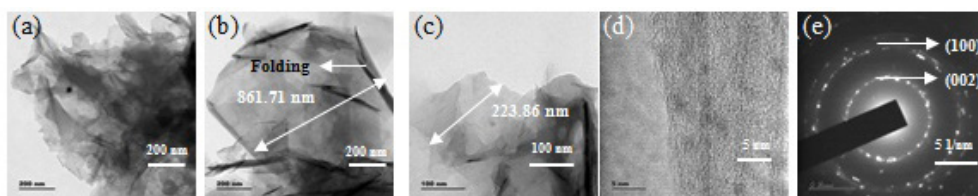


Figure 6. (a-d) Bright field HRTEM images and (e) SAED pattern of GnP.

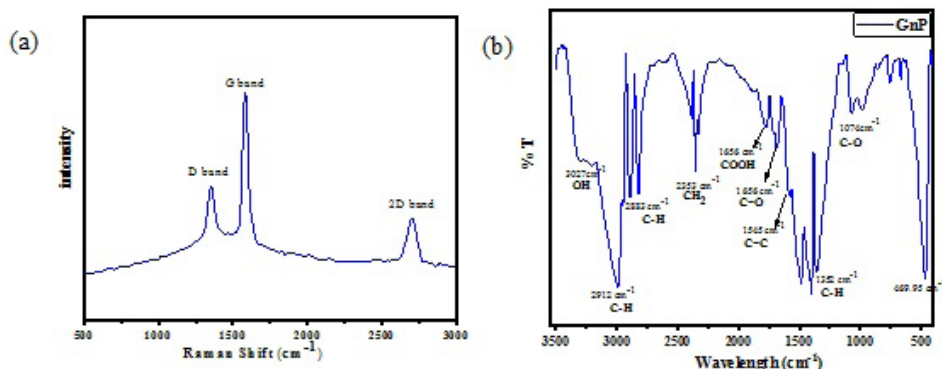


Figure 7. (a) Raman Spectroscopy and (b) FTIR of GnP.

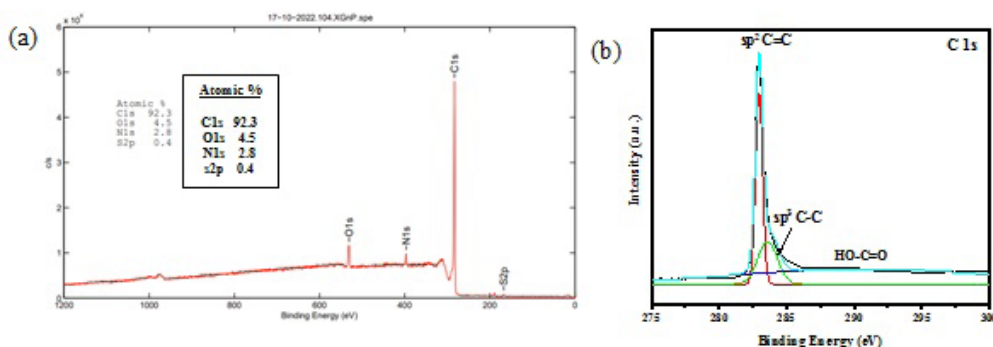


Figure 8. (a) XPS of GnP (b) XPS C 1s spectra of GnP.

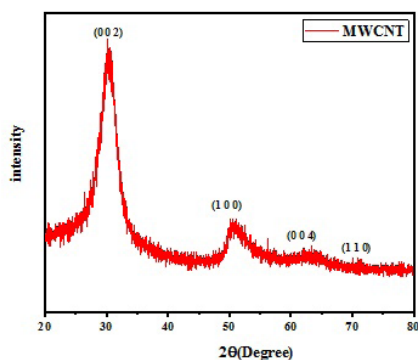


Figure 9. XRD of acid-functionalized MWCNT.

impurity in the Ar gas. The XPS spectrum of GnP did not contain any elements other than C and O clearly indicating the absence of impurities³⁴. Figure 9 is the XRD spectrum of the acid-functionalized MWCNTs in 2θ range of 20–80°. The sharp intense peaks in the XRD spectrum clearly indicate the crystalline nature of the MWCNTs. The XRD spectrum shows the (002), (100), (102), and (101) peaks corresponding to the hexagonal structure of the MWCNTs. The (002) peak corresponding to the basal plane of the MWCNTs was seen at 2θ value of 30.33°. The interplanar spacing of the (002) diffraction planes (d_{002}) calculated using the Bragg's law is ~ 3.4144 Å which is well within the range reported for pristine MWCNT in literature^{35,36}. From the XRD, it is evident that there is no impurity present in the MWCNT powder particles. The sharpness of the XRD peaks indicate that no significant damages have been done to the MWCNTs during acid-functionalization and ultrasonication which was done to deagglomerate and disentangle the MWCNT.

The SEM images in Figure 10a–10b show MWCNTs entangled due to their high aspect ratio. The MWCNTs have been acid-functionalized to modify them and enable interaction with the metal matrix and improve their dispersion in the metal matrix. In order to modify the MWCNTs the MWCNTs were treated with a mixture of sulphuric acid (H_2SO_4) and nitric acid (HNO_3) in the volume ratio of 1:3. Due to the hydroxyl (OH) and carboxylic (COOH) functional groups attached to the surface of the MWCNTs during functionalization, it was possible to break the strong Van der Waals forces between them and to prevent their agglomeration³⁷.

The HRTEM images in Figure 10c–10d show the structure of the MWCNTs. Figure 10d and with the image inset clearly show that the carbon nanotubes are multiwalled in nature. The outer diameter of the MWCNTs is in the range of 11–20 nm whereas their inner diameter is in the range of ~ 5 –7.5 nm. The SAED pattern in Figure 10e shows sharp concentric rings clearly indicating the high degree of crystallinity of the MWCNTs and confirm that the graphitic structure of the MWCNTs was preserved³⁸.

Raman spectroscopy provides a convenient and direct way to examine the quality of the MWCNTs. Figure 11a shows the Raman spectrum of the acid-functionalized MWCNT. The Raman spectrum of the MWCNT shows three characteristic G, D and 2D peaks. The G-band is the first order Raman mode and appears at ~ 1580 cm^{-1} and it is an intrinsic feature related to the vibrations in all sp^2 carbon atoms. The D-band comes from the second-order scattering process and occurs at around 1280–1350 cm^{-1} . It provides information about the structural defects and presence of amorphous carbon in the sample. The larger is the number of defects the higher is the D-band's intensity. The FTIR spectrum of the acid-functionalized MWCNTs in Figure 11b shows stretching vibrations due to carbonyl groups at 1679 cm^{-1} , while absorption bands at 1385 cm^{-1} and 1078 cm^{-1} are associated to hydroxyl (OH) group bending and alkoxy (C–O) stretching respectively³⁹.

The XPS analysis was done to analyse the various chemical bonds in the MWCNTs. The elemental analysis along with the XPS spectra of the MWCNTs in Figure 12a shows the presence of ~ 15.1 at. % O. This is due to the carboxylic (COOH) functional groups attached to the MWCNTs during acid-functionalization. During the acid-functionalization the MWCNTs were oxidized using an oxidative acid and this resulted in the attachment of the oxide functional groups to them. The Voigt function was used for the XPS peak deconvolution of the C 1s peak. The C 1s spectra is composed of several characteristic peaks, such as two peaks due to the C–C interactions including C=C sp^2 bonds at the binding energy of 284.4–284.7 eV and C–C sp^3 bonds at 285.1–285.5 eV, and a relatively weak peak due to the COOH functional group at 289–291.6 eV⁴⁰.

Large-scale synthesis of hBN nanoplatelets having few layers of hBN stacked together has been challenging, mainly due to the strong interlayer interactions occurring due to the electronegativity difference between the elemental components B and N⁴¹.

Here, in the present study, the exfoliation of commercially available hBN was carried out by a facile ball milling technique. The as-received pristine hBN were exfoliated by milling in a planetary ball mill for 20 h using toluene as the process controlling agent (PCA) during milling. Wet milling is an efficient and high-yield method to produce 2D nanomaterials, having high crystallinity if the milling conditions are optimized. The yield of exfoliated hBN by the milling process was high which is why this technique was adopted for the synthesis of the exfoliated hBN nanoplatelets. The XRD spectra of both the as-received pristine hBN and 20 h milled hBN in Figure 13a show peaks corresponding to the (002), (100), (101), (102) and (004) diffraction planes of hBN confirming its hexagonal structure. The XRD spectra of both as-received hBN and 20 h milled hBN show a strong intense peak corresponding to the (002) diffraction plane at 2θ value of 31.28° suggesting the high degree of crystallinity of hBN. The interplanar

distance (d_{002}) between the (002) planes calculated using the Bragg's law ($\lambda = 2d\sin\theta$) is 3.3180 \AA which is in close conformity with the d_{002} value reported in literature⁴⁰. The intensity of the (002) peak of hBN shows a slight decrease after milling for 20 h (Figure 13b). However, there is no measurable broadening of the (002) peak. This suggests that milling does not have a significant effect on the in-plane structure of hBN and the milled hBN nanoplatelets have a high degree of crystallinity. The XRD plots reveal that the intensity of the (004) peak has reduced considerably after 20 h of milling. This suggests significant reduction in the thickness in the c-direction of the hBN nanoplatelets. From the XRD spectra it is evident that the hBN does not have any impurity.

hBN nanoplatelets can be synthesized by bottom-up processes like chemical vapour deposition (CVD) or segregation method or by top-down processes like exfoliation of bulk hBN by mechanical processes like ball milling or ultrasonication.

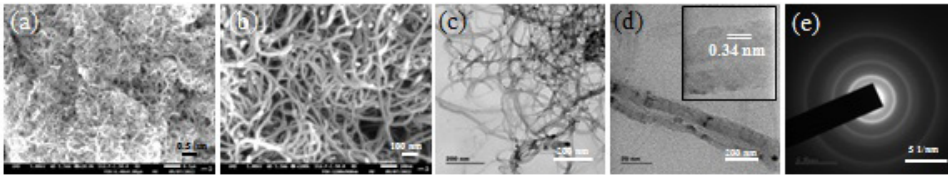


Figure 10. (a, b) SEM images (c, d) Bright field HRTEM images with d-spacing (e) SAED pattern of acid-functionalized MWCNT.

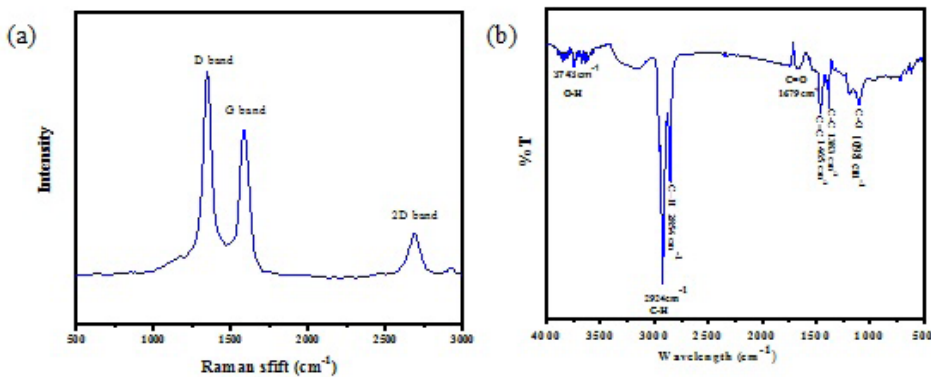


Figure 11. (a) Raman spectroscopy and (b) FTIR of acid-functionalized MWCNT.

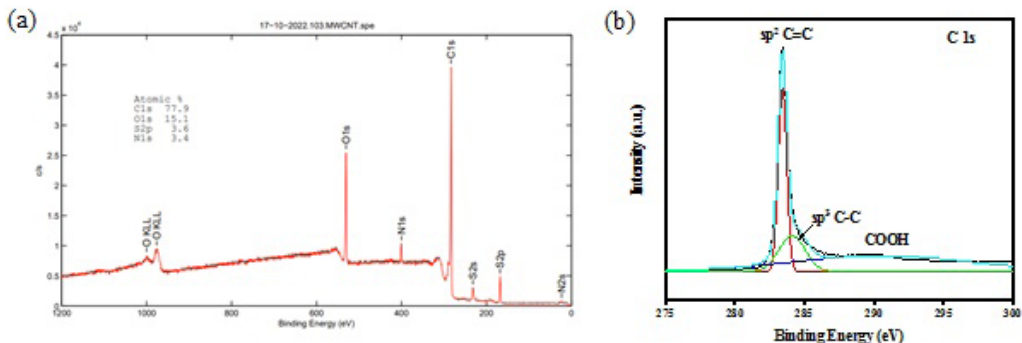


Figure 12. (a) XPS analysis of acid-functionalized MWCNT (b) XPS C 1s spectra of MWCNT.

Here, in the present work, the bulk pristine hBN has been exfoliated by ball milling for 20 h in a wet medium of toluene. After milling for 20 h, the hBN shows a reduction in lateral size and thickness (Figure 14). Milling disrupted the layered structures of the hBN, resulting in a significant increase of surface area which is also evident from the BET analysis. Within the initial period of milling, the hBN particles get delaminated and partially exfoliated by the shear force produced by the impact of the balls during milling. Due to the shear force, the weak interplanar bonds are broken and thinner hBN nanoplatelets having few layers of hBN stacked together were produced. There is also a possibility of functional groups getting attached to the hBN nanoplatelets during milling. The EDXS analysis of the 20 h milled hBN along with the SEM image in Figure 14f shows 12.82 at. %

O in it. Whereas no O was detected in the as-received hBN. This is due to the oxidation of the hBN nanoplatelets during milling forming diboron trioxide (B_2O_3) on its surface and its concentration has been reported to increase with the increase in milling time⁴¹. The presence of O in the hBN nanoplatelets has also been confirmed by XPS analysis. Figure 15 shows the HRTEM images of pristine hBN. The HRTEM image in Figure 15c of pristine hBN shows small, disc-like nanoplatelets having size in the range of ~ 0.1 -1 μm . The SAED pattern of pristine hBN in Figure 15e shows a hexagonal spot pattern. The SAED pattern in Figure 15j of the 20 h milled hBN shows concentric circles corresponding to the (002) and (100) diffraction planes of hBN with bright spots clearly indicating that the 20 h milled hBN nanoplatelets are well exfoliated^{42,43}.

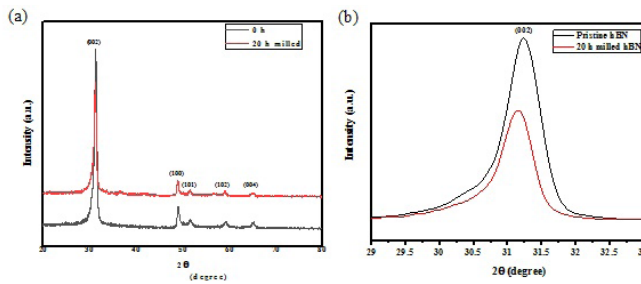


Figure 13. (a) XRD spectra and (b) (002) peak of pristine and 20 h milled hBN.

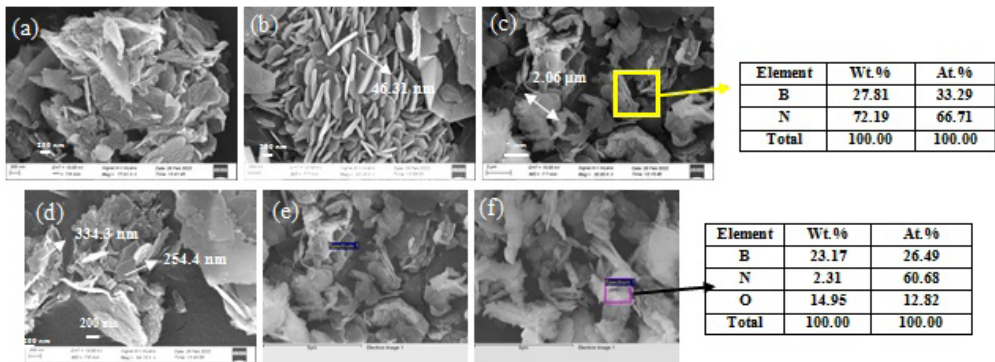


Figure 14. SEM images of (a-c) pristine hBN and (d-f) 20 h milled hBN with EDXS analysis.

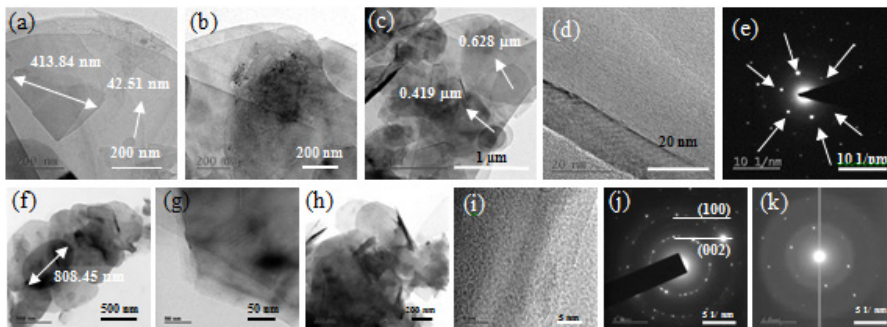


Figure 15. (a-d) Bright field HRTEM images and (e) SAED pattern of pristine hBN (f-i) Bright field HRTEM images and (j, k) SAED pattern of 20 h milled hBN.

Raman spectroscopy is an essential technique to characterize and investigate graphene and other 2D materials. The Raman spectra of as-received hBN and the 20 h milled hBN in Figure 16a show a sharp and intense peak at $\sim 1370\text{ cm}^{-1}$ corresponding to Raman-active high-energy phonon E_{2g} vibration mode. It should be noted that the E_{2g} Raman intensity of hBN is about 50 times weaker than that of graphene under similar conditions. This is the G-band of the hBN⁴⁴. Figure 16b shows the FTIR spectra of as-received and 20 h milled hBN samples. Both the spectra show two strong peaks at $\sim 813\text{ cm}^{-1}$ and $\sim 1379\text{ cm}^{-1}$ which are assigned to

the B-N-B bending vibrations and B-N stretching vibrations respectively. The absorption band at $\sim 3267\text{ cm}^{-1}$ seen in both the FTIR plots can be correlated to the stretching vibrations of the N-H group. The faint peak at $\sim 490\text{ cm}^{-1}$ seen in the FTIR spectrum of the 20 h milled hBN sample can be attributed to the negligible amount of B_2O_3 present in the hBN. This peak corresponds to the B-O-B vibration. B_2O_3 could be formed by the oxidation of B during milling as there is a chance of functional groups being attached to the surface of the hBN nanoplatelets. The presence of O in the 20 h milled hBN nanoplatelets was also confirmed by XPS (Figure 17).

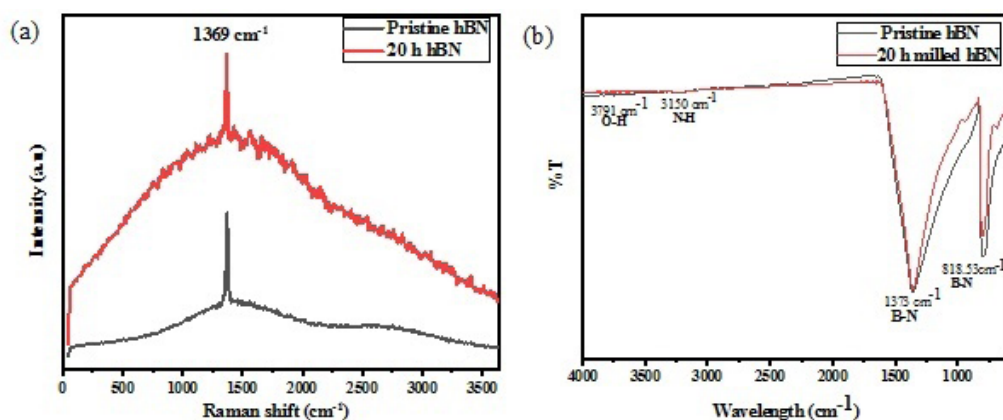


Figure 16. (a) Raman spectroscopy and (b) FTIR plot of hBN.

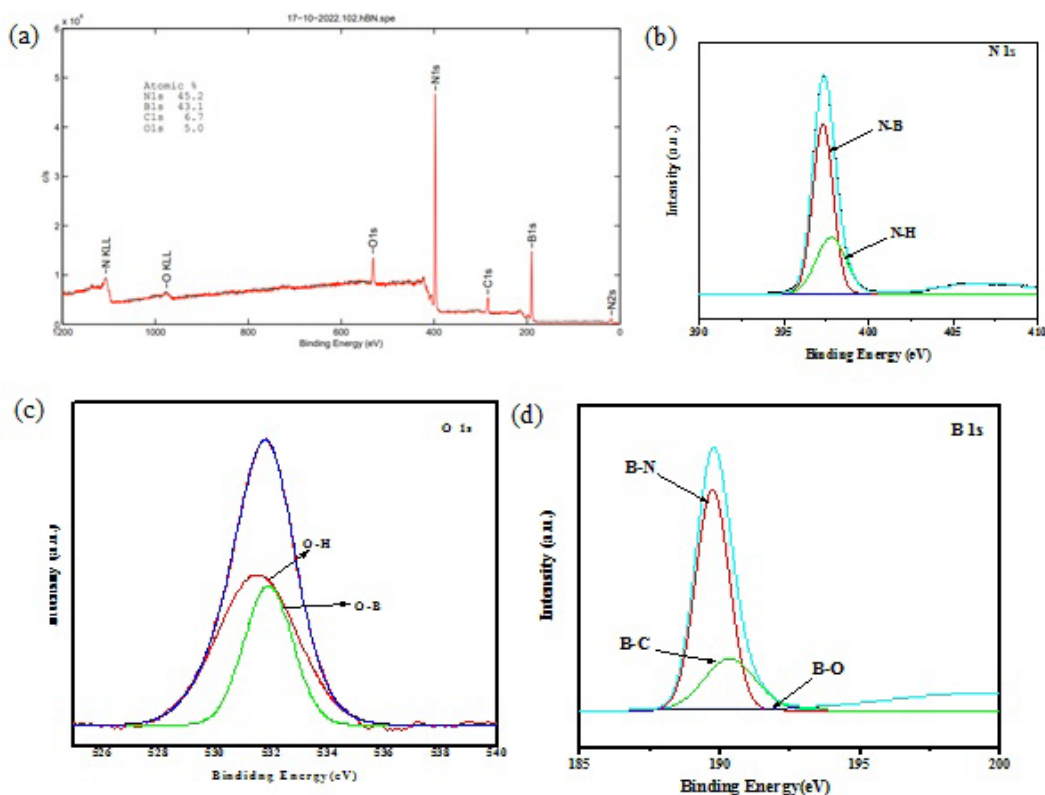


Figure 17. XPS analysis of 20 h milled hBN.

The FTIR analysis does not show any new peak suggesting that no new detectable amount of functional groups were attached to the surface of hBN after milling for 20 h⁴⁵.

The XPS analysis of the 20 h of milled hBN in Figure 17 shows that it is almost stoichiometric with very small amount of O (5 at. %) and C (6.7 at. %). The presence of C1s and O1s peaks in the survey spectrum of exfoliated hBN indicates that a small amount of impurity elements exists in the exfoliated hBN due to the adsorption of CO, H₂O and O₂ on the surface of the sample during milling. The presence of O acts adversely on the properties of hBN and it could be due to milling or due to the exposure of the hBN to air^{46,47}. The elemental composition of the 20 h milled hBN is 45.2 at. % N, 43.1 at. % B, 6.7 at. % C and 5 at. % O. The quantification of B1s and N1s peaks confirms the stoichiometry of 1.04: 1 for B: N and confirms that the pristine hBN is stoichiometric with very small amount of O in it which was bonded to the B atoms during milling. The N1s spectrum in Figure 17b exhibited a main peak at ~398.4 eV. The XPS spectra showed the presence of a single component at ~190.8 eV in the B1s spectrum assigned to the B-N bonds (Figure 17d). A small peak at 192 eV corresponding to B-O bonds comes from B-site hydroxylation.

Figure 18 shows the BET analysis of the as-received hBN and the 20 h milled hBN. The average pore diameter of the pristine as-received hBN was found to be 3.63 nm confirming the presence of mesopores in them and the surface area of pristine hBN was found to be 28.376 m²/gm. The pore volume was found to be 0.116 cc/gm. The average pore diameter of the 20 h milled hBN was found to be ~3.94 nm and the surface area was found to be ~37.16 m²/gm. The pore volume was found to be ~0.106 cc/gm. The presence

of mesopores in the 20 h milled hBN was confirmed by the BET analysis. Ball milling disrupted the layered structure of the 20 h milled hBN, resulting in significant increase in the surface area⁴⁸.

Figure 19a-19b are the SEM images of the CNT_{0.3}GnP_{0.3}hBN_{0.4} powder mixtures. The elemental maps of N and B in Figure 19d-19e indicate that the large particle in the centre of the SEM image in Figure 19b is that of hBN. The C in the background is due to the carbon tape on which the sample was placed. However, C could be seen lying over the hBN in the combined elemental map in Figure 19c indicating that the CNT-GnP are in close contact with the hBN. The elemental map of O in Figure 19g shows the presence of O in the CNT-GnP-hBN nanofiller. Due to the acid-functionalization of the MWCNTs oxygen containing groups like carboxylic group (COOH) and hydroxyl group (OH) were attached to the MWCNTs. The COOH functional group was also present in the GnP as the GIC was synthesized by adding H₂SO₄ and strong oxidizing agents like H₂O₂ to the NFG^{49,50}.

Figure 20 shows HRTEM images of GnP and hBN stacked together in the CNT_{0.3}GnP_{0.3}hBN_{0.4} powder mixture. The electronegativities of B(2.04), C(2.55) and N(3.04) are different and this could also stabilize the stacking of GnP and hBN over one another. The AA' stacking mode of hBN is also stabilized due to the similar reason where B atoms bearing a partial positive charge in one layer resides on top of the oppositely charged N atoms on the adjacent layers⁵¹. Similarly the difference in the electronegativities of B, N and C could also stabilize the stacking of the GnP on the hBN nanoplatelets. The HRTEM micrographs in Figure 20 clearly show the plate like layered morphology of the GnP and hBN in the hybrid nanofiller which are also transparent to

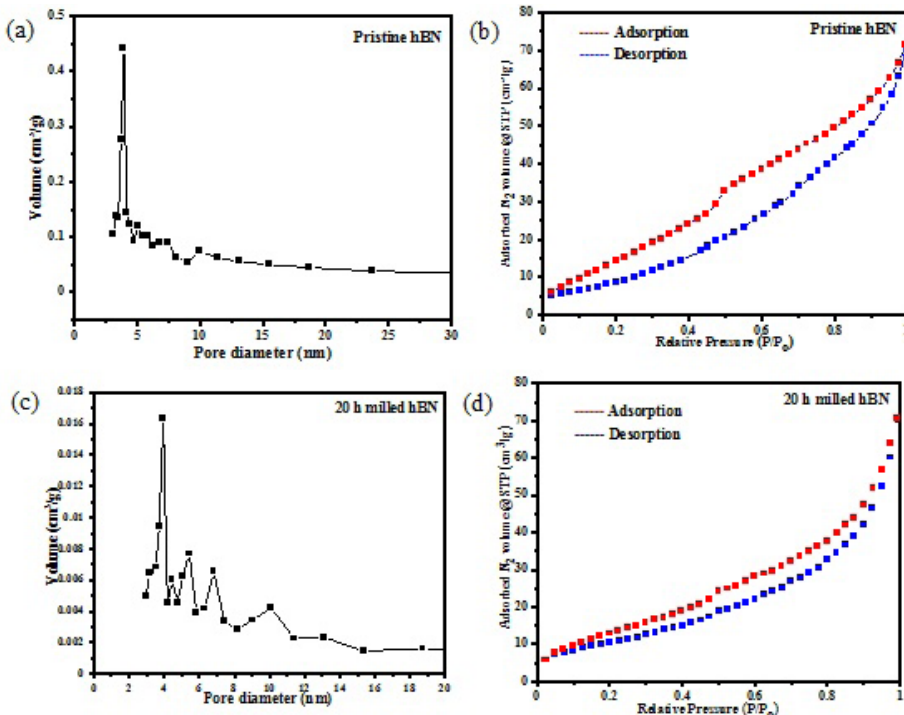


Figure 18. BET analysis of (a, b) as-received hBN (c, d) 20 h milled hBN.

the electron beam. Parallel lattice fringes with an interlayer spacing of $d_{002} = 0.344$ nm corresponding to the (002) planes of MWCNT can be seen in Figure 20d⁵². The SAED patterns in Figure 20e, 20j show fuzzy and discontinuous rings which manifests the polycrystalline nature of the hBN.

The integration of the three nanofillers to form a 3D hybrid structure was achieved by ultrasonication the nanofillers in the desired weight fractions. The intercalation of the MWCNTs between the hBN and the GnP nanoplatelets could provide a 3D structure resulting in a more efficient load transfer than the individual nanofiller. The synergistic effect provided by the CNT-GnP-hBN ternary hybrid nanofiller could be highly efficient and could enhance the mechanical properties and wear behaviour of the nanocomposites. The 2D hBN and GnP would be stacked over each in the hybrid nanofiller and would form an in-plane junction between them. The difference in electronegativities between C, B and N could also result in stacking of GnP and hBN nanoplatelets on each other. As the mechanical properties of the three nanofillers are similar their arrangement in the hybrid nanofiller would determine the load transfer from the metal matrix to the hybrid nanofiller. The HRTEM images in Figure 20 show 2D GnP and hBN nanoplatelets entangled with the 1D MWCNT and forming a compact and overlapping network. The MWCNTs act as spacers between the 2D nanofillers and interrupted the dense

packing between the hBN and GnP particles and reduced the packing between them. Due to their large aspect ratio the MWCNTs get entangled with each other and the Al particles as well as the GnP and the hBN nanoplatelets get entrapped in them during ultrasonication. The exfoliation of hBN was more difficult than GnP due to which the hBN nanoplatelets were found to have more number of hBN layers stacked together than in GnP. The GnP nanoplatelets are much thinner than the hBN nanoplatelets and are therefore more flexible and would be more easily wrapped around the Al particles than the hBN nanoplatelets. This could also affect the densification of the Al-based nanocomposites when the hBN nanoplatelets are present at a higher loading level in the Al matrix^{53,54}. Figure 21a-21b shows the DSC/TGA plots of CNT_{0.3}GnP_{0.3}hBN_{0.4} and CNT_{0.3}GnP_{0.3}hBN_{4.4} powder mixtures. The shallow endothermic peak in initial part of both the DSC plots is due to the evaporation of the adsorbed moisture, toluene or acetone. Toluene was used as a process control agent during milling for exfoliating the hBN whereas acetone was used for ultrasonication for blending the powder mixtures. The evaporation of these adsorbed liquids was accompanied with the loss in mass. This was observed upto a temperature of $\sim 400^\circ\text{C}$. The net loss in mass after heating upto 1200°C was $\sim 7.75\%$ in the case of CNT_{0.3}GnP_{0.3}hBN_{0.4} powder mixture and $\sim 3.89\%$ in the case of CNT_{0.3}GnP_{0.3}hBN_{4.4} powder mixture.

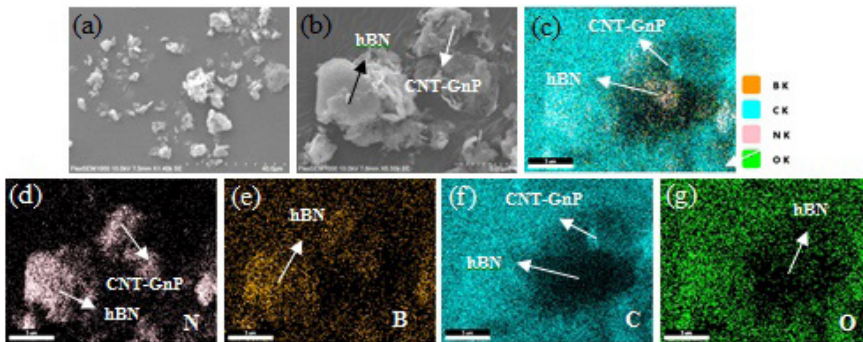


Figure 19. (a, b) SEM images (c) combined elemental map and elemental map of (d) N (e) B (f) C and (g) O in CNT_{0.3}GnP_{0.3}hBN_{0.4} powder mixture.

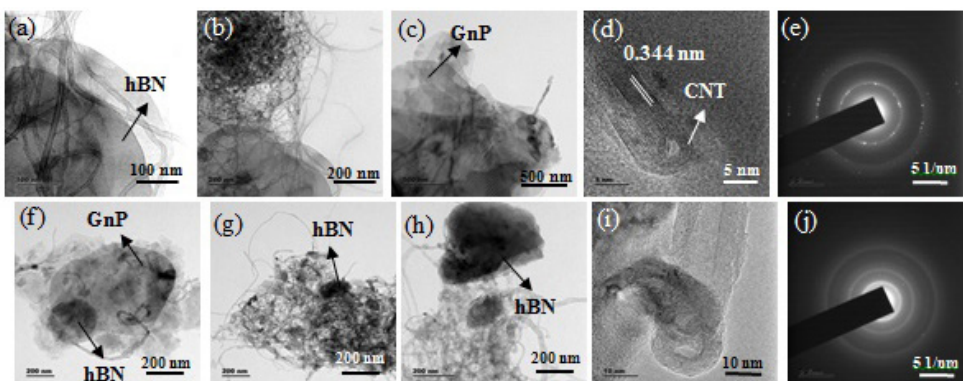


Figure 20. (a-d) HRTEM images and (e) SAED pattern of CNT_{0.3}GnP_{0.3}hBN_{0.4} and (f-i) HRTEM images and (j) SAED pattern of CNT_{0.3}GnP_{0.3}hBN_{4.4} powder mixtures.

Heating beyond $\sim 600^\circ\text{C}$ results in the degradation and combustion of the carbonaceous nanofillers, MWCNT and GnP, forming gaseous products like CO and CO_2 . However, hBN has very high thermal stability of upto $\sim 1000^\circ\text{C}$ and gets oxidized forming B_2O_3 on the hBN nanoplatelets in the temperature range of $1000\text{--}1200^\circ\text{C}$ ⁵⁵. In the case of $\text{CNT}_{0.3}\text{GnP}_{0.3}\text{hBN}_{0.4}$ powder mixture the weight fraction of the carbonaceous nanofiller is lower than hBN. Therefore, we see a lesser extent of loss in mass as compared to $\text{CNT}_{0.3}\text{GnP}_{0.3}\text{hBN}_{0.4}$. Also due to the higher thermal stability of the hBN it protects the MWCNT and GnP from thermal degradation and combustion which is why we see a very low loss in mass after thermal analysis upto 1200°C ⁵⁶. Crystalline B_2O_3 has a melting point of 450°C . However, amorphous boron oxide does not have a specific melting point and begins to melt at 325°C and becomes fluid at 500°C . Therefore, the endothermic peak which starts at $\sim 400^\circ\text{C}$ seen in both the DSC curves can be attributed to the melting of the B_2O_3 ⁵⁷.

The elemental maps of Al (Figure 22d) and O (Figure 22e) are very similar and clearly indicate the oxidation of the Al metal powder. The oxidation of Al has also been confirmed by the XRD and EDXS analysis. The elemental maps of B and N in Figure 22f and Figure 22g respectively also suggest close association of the hBN with the Al particles and confirm that a proper blending between the ternary nanofiller and the Al powder could be achieved by ultrasonication. The hBN nanoplatelets can be seen lying over the Al particle in Figure 22d and covering the Al particle completely. The SEM image in Figure 22c shows MWCNT wrapped around the Al particle. All the SEM images in Figure 22a-22c show that the ternary hybrid nanofiller is well dispersed within the Al powder and is in close contact with the Al particles.

Figure 23a-23c are the HRTEM images of the Al-1 wt.% $\text{CNT}_{0.3}\text{GnP}_{0.3}\text{hBN}_{0.4}$ powder mixture. The hBN nanoplatelets are darker in colour in the HRTEM images as they have a larger number of hBN layers stacked together as compared to the GnP.

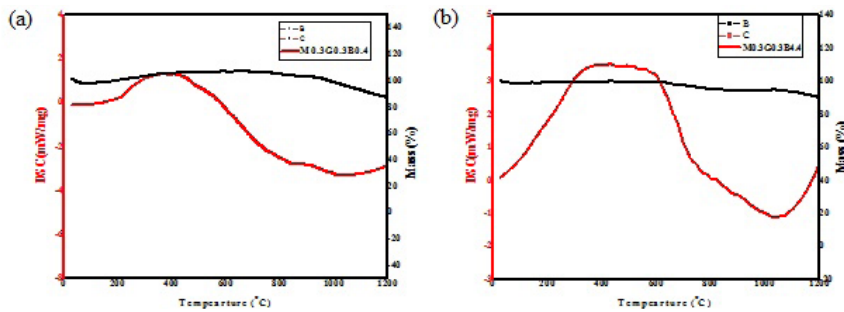


Figure 21. DSC and TGA of (a) $\text{CNT}_{0.3}\text{GnP}_{0.3}\text{hBN}_{0.4}$ (b) $\text{CNT}_{0.3}\text{GnP}_{0.3}\text{hBN}_{0.4}$ powder mixture.

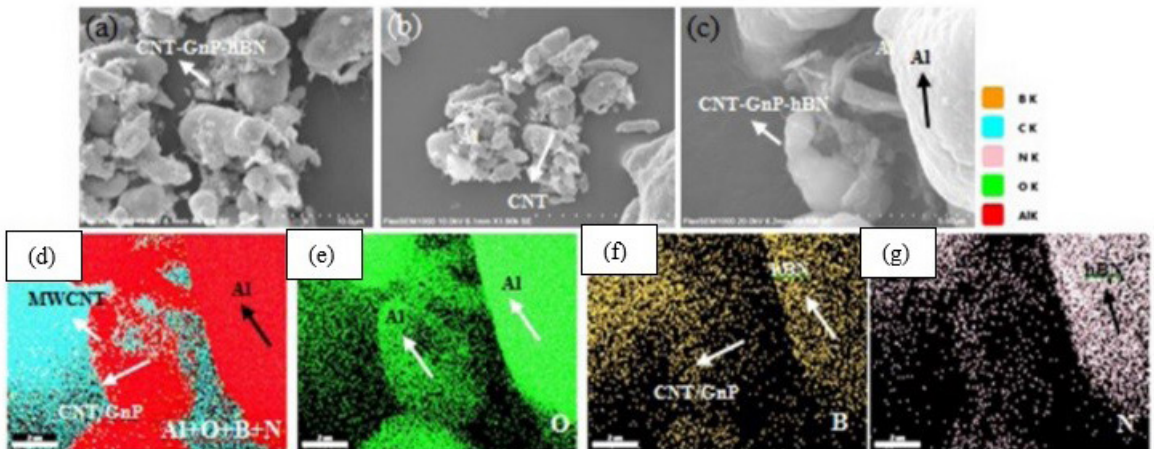


Figure 22. (a-c) SEM images (d) combined elemental map and elemental maps of (e) O, (f) B and (g) N in Al-1 wt.% $\text{CNT}_{0.3}\text{GnP}_{0.3}\text{hBN}_{0.4}$ powder mixture.

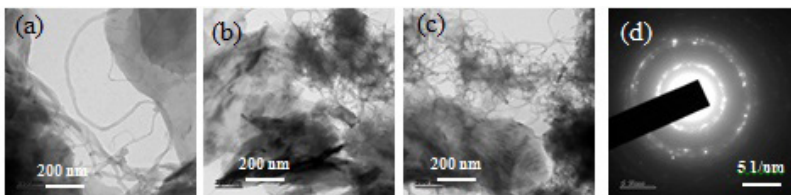


Figure 23. (a-c) HRTEM images (d) SAED pattern of Al-1 wt.% $\text{CNT}_{0.3}\text{GnP}_{0.3}\text{hBN}_{0.4}$ powder mixture.

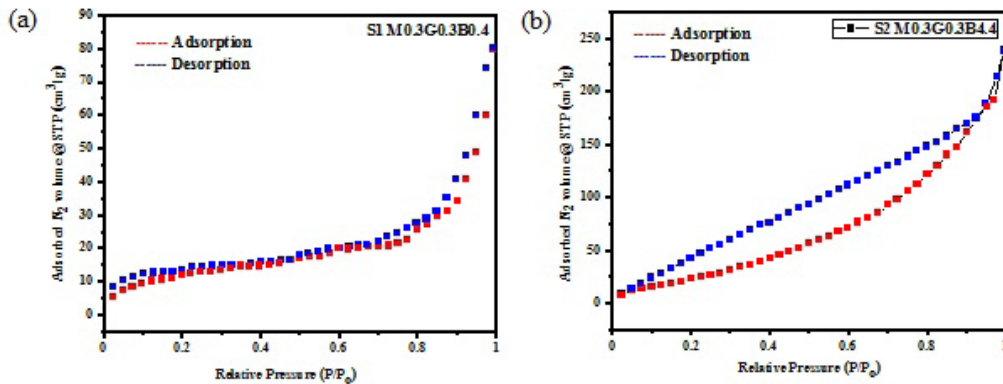


Figure 24. BET analysis of (a) Al-1 wt.% CNT_{0.3}GnP_{0.3}hBN_{0.4} and (b) Al-5 wt.% CNT_{0.3}GnP_{0.3}hBN_{4.4} powder mixture.

It was seen earlier that as hBN was more difficult to exfoliate than GnP the number of layers in the hBN nanoplatelets are higher as compared to that in GnP. The GnP are more transparent to the electron beam than the hBN. The hBN nanoplatelets have rounded edges whereas the GnP have straight and sharp edges. The HRTEM images show that a proper blending between the three nanofillers and the Al metal powder has taken place by ultrasonication. The GnP and hBN nanofillers are found trapped within the CNTs (Figure 23c). There is proper contact between the three nanofillers although the MWCNTs show a tendency to get entangled and form bundles due to their high aspect ratio. Few dark regions formed by the agglomerates of the nanofiller and Al powder could be seen in the HRTEM images. The sharp concentric rings in the SAED pattern in Figure 23d confirm the highly crystalline nature of the nanofillers. The structural integrity of the nanofillers was preserved even after blending by ultrasonication. Figure 24 shows the BET analysis of the Al-1 wt.% CNT_{0.3}GnP_{0.3}hBN_{0.4} and Al-5 wt.% CNT_{0.3}GnP_{0.3}hBN_{4.4} powder mixtures. The surface area of Al-1 wt.% CNT_{0.3}GnP_{0.3}hBN_{0.4} powder mixture was found to be 51.181 m²/gm and its pore volume was found to be 0.118 cc/gm. The pore diameter was 3.926 nm. On the other hand, the surface area of Al-5 wt.% CNT_{0.3}GnP_{0.3}hBN_{4.4} powder mixture was 73.447 m²/gm. The pore volume of the powder mixture was 0.348 cc/gm and its pore diameter was found to be 2.974 nm. With the increase in the loading level of hBN there is a significant increase in the surface area. However, an increase in the pore volume and pore diameter was also observed with the increase in the loading level of hBN in the hybrid nanofiller. This is also the reason why the relative density of the Al-CNT-GnP-hBN nanocomposite reduces with the increase in the loading level of the hBN⁵⁸.

Figure 25 shows the XRD spectrum of the as-received pure Al metal powder. The XRD spectrum of pure Al shows peaks corresponding to the (111), (002), (220), and (113) diffraction planes of FCC Al. A faint low intensity peak corresponding to aluminium oxide (Al₂O₃) could also be seen in the XRD spectrum. The XRD peak of Al₂O₃ is almost undetectable due to the trace amount of Al₂O₃. The formation of Al₂O₃ is due to the mild oxidation of the Al metal powder which takes place due to the unavoidable exposure of the powder to open atmosphere. Al has a strong affinity for oxygen forming a thin layer of dense, compact Al₂O₃ which protects the bulk metal underneath from further oxidation⁵⁹.

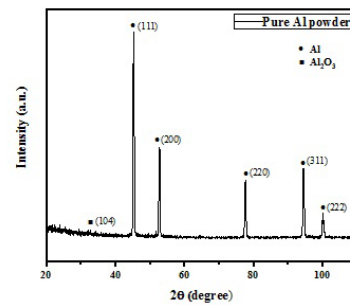


Figure 25. XRD of as-revived pure Al powder.

The SEM image in Figure 26 show the dumbbell shaped Al particles in the as-received pure Al powder. These particles have a size in the range of ~10-50 μm. Very fine Al particles having a size of few microns as well as large-sized Al particles having a size of upto ~50 μm can be seen in the SEM images. The EDXS analysis given along with the SEM image in Figure 26 shows the presence of 7.51 at. % O in the Al particles. Both the EDXS analysis of the pure Al powder in Figure 26 as well as the XRD spectrum of the pure Al powder in Figure 25 clearly suggests that the extent of oxidation of Al is very low.

Figure 27b shows the XRD spectra of Al-1, 2, 3 and 5 wt. % CNT-GnP-hBN hybrid nanocomposites. All the XRD spectra show peaks corresponding to the various diffraction planes of FCC Al. A low intensity peak corresponding to the (002) peak of the CNT-GnP-hBN ternary hybrid nanofiller could be seen at 2θ value of 32.086°. It should be noted that the (002) peak of MWCNT, GnP and hBN are very close to each other at 2θ values of 30.33, 30.99 and 31.28° respectively and therefore overlap with each other. From Figure 27d it has evident that increasing the loading level of hBN in the ternary hybrid nanofiller increases the intensity of the (002) peak. The highest intensity of the (002) peak was seen in the case of Al-5 wt.% CNT_{0.3}GnP_{0.3}hBN_{4.4} hybrid nanocomposite. The peak corresponding to the (104) diffraction plane of Al₂O₃ could be seen at 2θ value of 33.42°. Al₂O₃ was earlier detected in the as-received Al powder both by XRD (Figure 25) and EDXS (Figure 26) analysis. Oxidation of Al could have also taken place by the residual oxygen present as impurity in the Ar gas used for sintering in the tubular furnace.

The strongest peak of Al_2O_3 was observed in the XRD spectrum of Al-5 wt.% $\text{GnP}_{0.3}\text{MWCNT}_{0.3}\text{hBN}_{4.4}$ nanocomposite. No peak corresponding to aluminium carbide (Al_4C_3) could be seen in the XRD spectra of the Al-based nanocomposites although the binary phase diagram of the Al-C system (Figure 2a) predicts the formation of intermetallic Al_4C_3 by the reaction of the Al matrix and the carbonaceous nanofillers in the ternary hybrid nanofiller. However, it should be noted that the amount of Al_4C_3 could be negligible and was not detected in the XRD spectra. The plot in Figure 27c shows the Al (111) peak in the various XRD spectra of the Al-based nanocomposites. A slight shift of the Al (111) peak towards the higher 2θ values could be seen with respect to the Al (111) peak of the sintered pure Al sample clearly indicating that there was slight diffusion of impurity atoms like C, B, N and O into the Al lattice. It should be noted that C(0.67 Å),

B(0.87 Å), N(0.56 Å) and O(0.48 Å) have a smaller atomic radius as compared to Al(1.18 Å) and their diffusion into the Al lattice could cause a shift of the Al peak towards higher 2θ values⁶⁰.

Figure 28 shows the optical micrographs of the sintered pure Al as well as the various Al-based nanocomposites developed by sintering at 550°C in Ar atmosphere for 2 h in a tubular furnace. The sintered nanocomposite samples were polished using Keller's reagent. A lower loading level of the ternary nanofiller in the Al matrix in the case of Al-1 wt.% $\text{CNT}_{0.3}\text{GnP}_{0.3}\text{hBN}_{0.4}$ nanocomposite resulted in a homogeneous distribution of the nanofiller (Figure 28c-28d). Beyond the loading level of 1 wt.% hybrid nanofiller in the Al matrix, agglomeration of the hybrid nanofiller was seen at the Al grain boundaries. A higher weight fraction of hBN in the ternary hybrid nanofiller resulted in the deterioration of the densification of the samples.

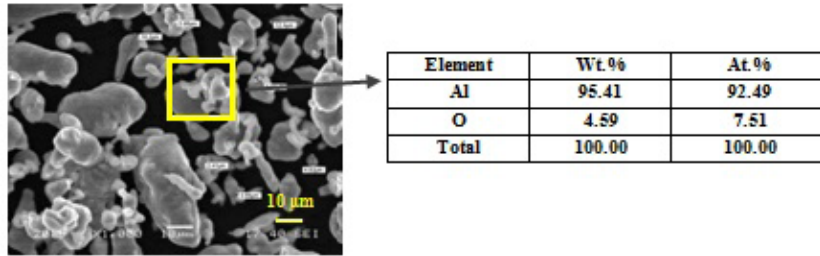


Figure 26. SEM image of pure Al powder along with EDXS analysis.

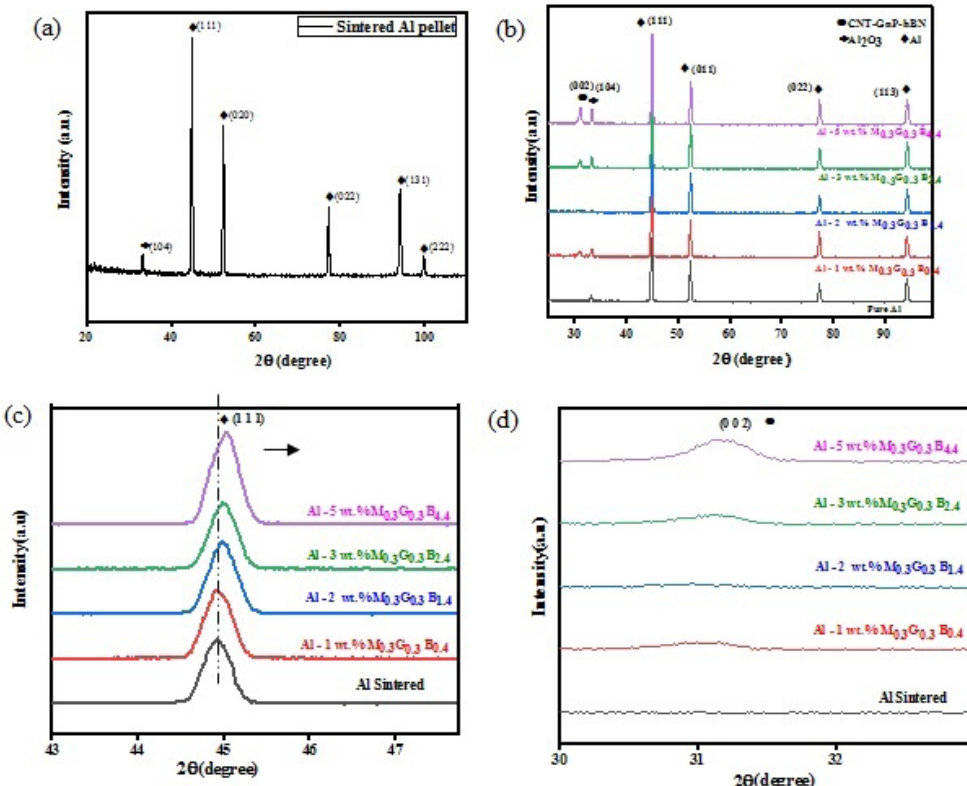


Figure 27. XRD of (a) pure Al and (b) Al-1, 2, 3, and 5 wt.% CNT-GnP-hBN nanocomposites (c) Al(111) peak and (d) (002) peak of CNT-GnP-hBN in Al-CNT-GnP-hBN nanocomposites.

The percentage of porosity increases with the increase in the loading level of the ternary hybrid nanofiller in the Al-based nanocomposites from ~7.43% in the case of Al-1 wt.% CNT-GnP-hBN nanocomposite to ~13.75% in the case of Al-5 wt.% CNT-GnP-hBN nanocomposite. Agglomerated hybrid nanofillers may act as a defect and thereby contribute to the occurrence of microcracks within the nanocomposite. When present in adequate amount the hybrid nanofiller can absorb the fracture energy and can alter the direction of crack propagation and stop crack propagation. It can enable crack pinning along the original direction. It should be noted that a uniform distribution of the nanofiller in the Al matrix can result in better mechanical properties due to grain refinement and Orowan strengthening mechanism. The Orowan strengthening mechanism is a significant strengthening mechanism in nanocomposites and dominantly affects their performance. In the Orowan strengthening mechanism closely associated hard nanosized particles

obstruct the movement of the dislocations. The dispersed strengthening and precipitation strengthening mechanisms are governed by Orowan dislocation bypassing or by the dislocation shearing mechanism. Therefore, a higher strength of the nanocomposites can be achieved by better nanofiller dispersion in the Al matrix. Figure 28g is a schematic diagram explaining the Orowan strengthening mechanism⁶¹⁻⁶³.

The SEM image of pure Al sample in Figure 29a developed under similar condition show large number of pores. Sintering of Al powder is known to be a difficult process, due to the tenacious oxide film present on the surface of the Al particles. The SEM images in Figure 29b of Al-1 wt.% CNT_{0.03}GnP_{0.03}hBN_{0.4} nanocomposite shows the uniform distribution of the hybrid nanofiller in the Al matrix. However, agglomerates of hBN can be seen in the SEM image of Al-3 wt.% CNT_{0.3}GnP_{0.3}hBN_{2.4} nanocomposite at the Al grain boundaries in Figure 29c when the loading level of the ternary hybrid nanofiller is higher than 1 wt.%.

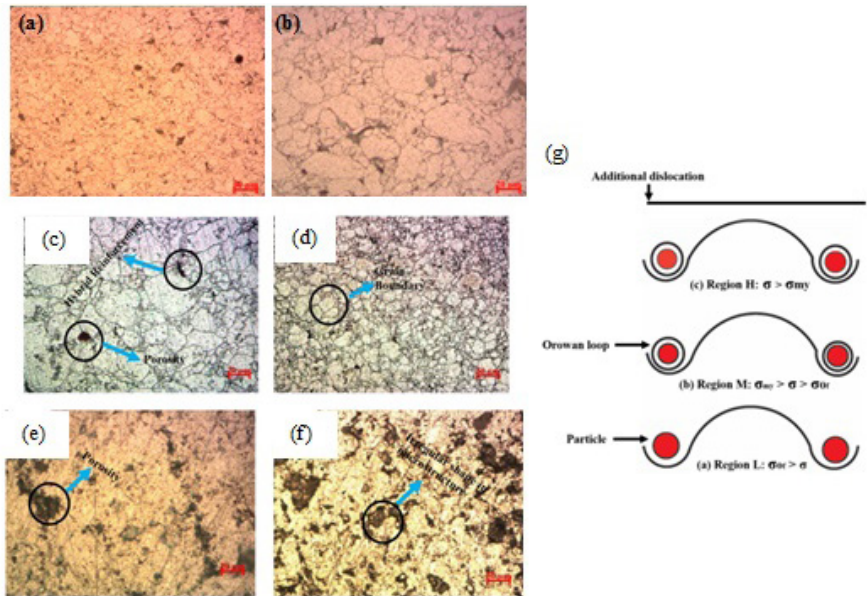


Figure 28. Optical micrographs of (a, b) sintered pure Al (c, d) Al-1 wt.% nanocomposite (e, f) Al-3 wt.% nanocomposite (g) Schematic diagram of Orowan strengthening mechanism.

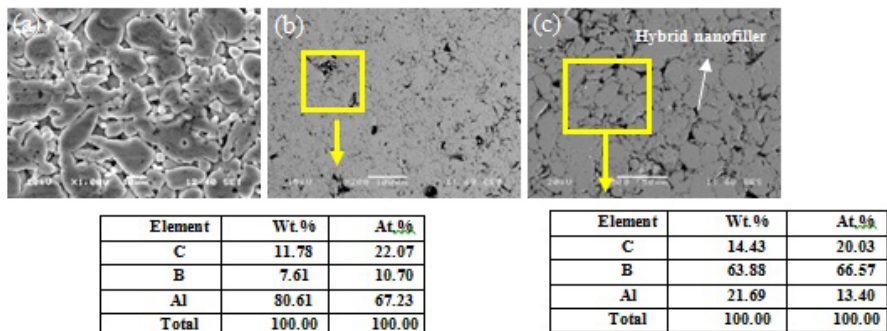


Figure 29. (a) SEM images of sintered pure Al sample. SEM images with EDXS analysis of (b) Al-1 wt.% CNT_{0.3}GnP_{0.3}hBN_{0.4} (c) Al-3 wt.% CNT_{0.3}GnP_{0.3}hBN_{2.4} nanocomposite.

The higher weight fraction of hBN in the ternary hybrid nanofiller did not improve the densification of the nanocomposite. The agglomeration of this ternary hybrid nanofiller containing higher amount of hBN led to the increase in the porosity of the sintered nanocomposite which eventually led to a decrease in the density of the nanocomposites. The relative density of Al-1 wt.% CNT_{0.3}GnP_{0.3}hBN_{0.4} nanocomposite was found to be highest among all the Al-CNT-GnP-hBN nanocomposites and was about ~5.01% times higher than that of the pure Al sample developed similarly. No reaction product was formed at the interface of the hybrid nanofiller and the Al matrix. This was also confirmed by the XRD plots in Figure 27b although formation of intermetallics like Al₄C₃ between Al and C, Al₂B₃ between Al and B and AlN between Al and N is predicted from the binary phase diagrams of the Al-C, Al-B and AlN systems in Figure 2. Figure 30a-30e show the HRTEM images of Al-1 wt.% CNT_{0.3}GnP_{0.3}hBN_{0.4} nanocomposites⁶⁴. The HRTEM images clearly show the ternary hybrid nanofiller embedded within the Al matrix at the grain boundaries. A large number of dislocations could also be seen. Figure 30c shows a large number of dislocations piled up at the grain boundaries where agglomerates of the ternary hybrid nanofiller are present. The SAED pattern in Figure 30f shows sharp rings corresponding to the polycrystalline Al matrix along with bright spots corresponding to the hybrid nanofiller. Figure 31a shows the variation of sintered density

and relative density of Al- CNT-GnP-hBN nanocomposites with the variation in the composition of the ternary hybrid nanofiller. It is evident from the plots that the highest relative density of ~92.56% was achieved in the case of Al-1 wt.% CNT_{0.3}GnP_{0.3}hBN_{0.4} nanocomposite. At a lower loading level of the ternary hybrid nanofiller a uniform distribution of the hybrid nanofiller in the Al matrix was observed. This resulted in better densification of the nanocomposites. Agglomeration of the ternary hybrid nanofiller adversely affected the sinterability of the nanocomposites. Increasing the loading level of the hBN nanofiller in the ternary hybrid nanofiller deteriorated the densification of the Al-based hybrid nanocomposite and resulted in lower relative density of the nanocomposites. With the increase in the loading level of hBN the agglomeration of hBN in the Al matrix takes place which also deteriorated the mechanical properties of the nanocomposites. Due to the microporous structure and agglomeration of the ternary hybrid nanofiller at higher loading level the hardness of the nanocomposite was also reduced. As the thermal decomposition of both the MWCNT and GnP starts beyond ~600°C and the hBN shows thermal stability upto a temperature of ~1000°C the structural integrity of all the nanofillers are expected to be preserved during the sintering which was carried out at 500°C for 2 h in Ar atmosphere. From Figure 31b it is evident that a significantly higher relative density could be achieved in the case of Al-hBN nanocomposites.

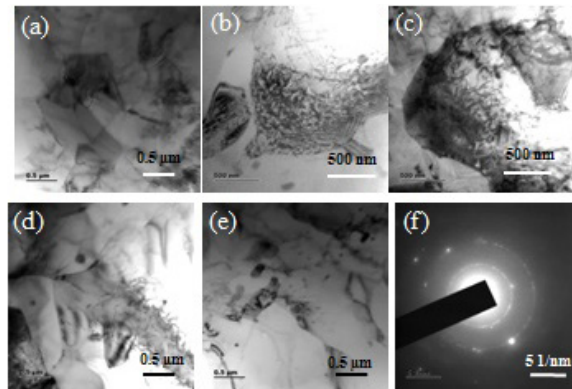


Figure 30. (a-e) HRTEM images (f) SAED pattern of Al-1 wt.% CNT_{0.3}GnP_{0.3}hBN_{0.4} nanocomposite.

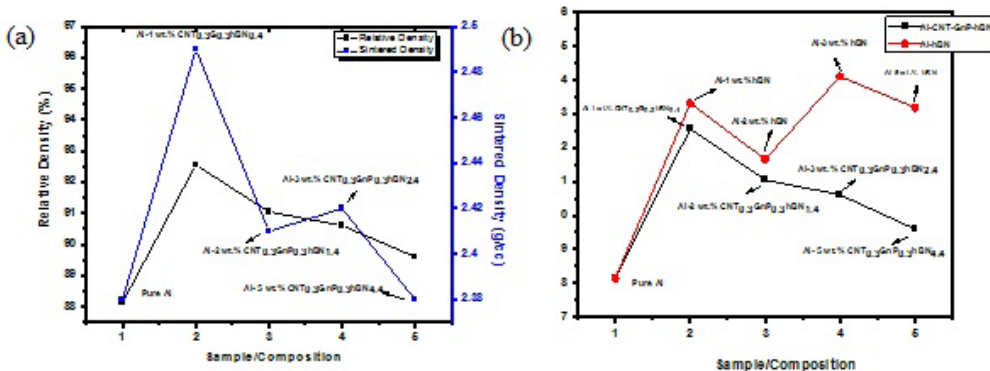


Figure 31. (a) Variation of sintered density and relative density of Al-CNT-GnP-hBN nanocomposites (b) Variation of relative density of Al-CNT-GnP-hBN and Al-hBN nanocomposites.

However, when the ternary hybrid nanofiller is added to the Al matrix the relative density of the nanocomposites is lower. This can be attributed to the mismatch in the properties of the three nanofillers which affects their sinterability. However, it should be noted that a higher relative density as compared to that of the pure Al sample (~88.14%) could be achieved in the case of all the Al-hBN and Al-CNT-GnP-hBN nanocomposites. The highest relative density achieved in the case of Al-CNT-GnP-hBN nanocomposites was for Al-1 wt.% CNT_{0.3}GnP_{0.3}hBN_{0.4} nanocomposite (~92.56%) which was slightly lower than the highest relative density achieved in the case of Al-hBN nanocomposites for Al-3 wt.% hBN nanocomposite (~94.11%)^{20,65}. Figure 32 shows the variation in hardness of Al-CNT-GnP-hBN and Al-hBN nanocomposites. The maximum hardness in the case of Al-CNT-GnP-hBN nanocomposites is observed in the case of Al-1 wt.% CNT_{0.03}GnP_{0.03}hBN_{0.4} nanocomposite (~415.91 MPa) whereas the maximum hardness in the case of Al-hBN nanocomposites is seen in the case of Al-3 wt.% hBN nanocomposite (~450.54 MPa). The maximum hardness achieved in the case of Al-CNT-GnP-hBN nanocomposites is slightly lower than that achieved in the case of Al-hBN nanocomposites. However, it should be noted that the hardness achieved in the case of all the ternary hybrid reinforced or monoreinforced nanocomposites is higher than that of the pure Al sample (~322.35 MPa) developed similarly⁶⁶.

Dry sliding wear test of the sintered pure Al and the various Al-based nanocomposites was done in order to determine the effect of the CNT-GnP-hBN ternary hybrid nanofiller on the wear resistance of the nanocomposites,

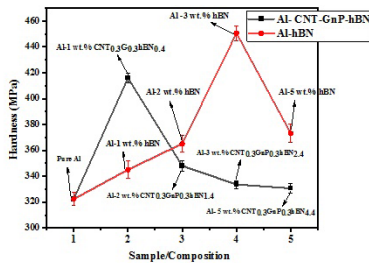


Figure 32. Variation of hardness of the Al-based nanocomposites.

and for comparison, the wear behaviours of the sintered pure Al and Al-hBN nanocomposites developed similarly has also been reported^{20,67}. A wear test can predict the performance and mechanism of wear. Ceramic reinforcements reduce wear to a considerable extent, but they increase the counter surface wear, due to which the lifecycle of the tribopair is reduced. The use of hybrid nanofillers like CNT-GnP-hBN can help easy shearing over the sliding surface, thereby reducing friction by forming a tribolayer. Figure 33a shows the variation in the wear depth of sintered pure Al and Al-CNT-GnP-hBN nanocomposites. Among the various nanocomposites, Al-1 wt.% CNT_{0.3}GnP_{0.3}hBN_{0.4} nanocomposite shows the least wear depth as well as the least wear rate (Figure 33b) and the highest improvement in wear resistance. Increasing the loading level of the CNT-GnP-hBN ternary hybrid nanofiller in the Al metal matrix from 1 wt.% to 3 wt.% by fixing the loading level of CNT and GnP and varying the loading level of the hBN deteriorated the wear resistance of the Al-based hybrid nanocomposites. Both the wear depth as well as the wear rate increase with the increase in the loading level of the hBN in the ternary hybrid nanofiller, thereby increasing the loading level of the ternary hybrid nanofiller in the Al matrix. This can be attributed to the agglomeration of the nanofiller in the Al matrix with the increase in the loading level of the hybrid nanofiller. Increasing the hBN loading level beyond 0.4 wt.% did not improve the wear resistance of the nanocomposite. Beyond the addition of 1 wt.% of the hybrid nanofiller, the wear properties of the nanocomposite deteriorated. However, it should be noted that the extent of wear shown by various Al-CNT-GnP-hBN nanocomposites was lower than that shown by the sintered pure Al sample as well as the Al-hBN nanocomposites developed similarly. This clearly indicates that adding CNT and GnP can enhance the wear resistance of the Al-based nanocomposites much more effectively than the hBN nanofiller. It can be seen from Figure 33a that, upto the addition of 3 wt.% of the CNT-GnP-hBN ternary hybrid nanofiller a significantly higher wear resistance of the Al-based hybrid nanocomposite was achieved as compared to the Al-hBN nanocomposites developed similarly, clearly indicating that the ternary hybrid nanofiller is more effective as compared to the hBN monofiller in improving the wear resistance of the Al-based hybrid nanocomposite.

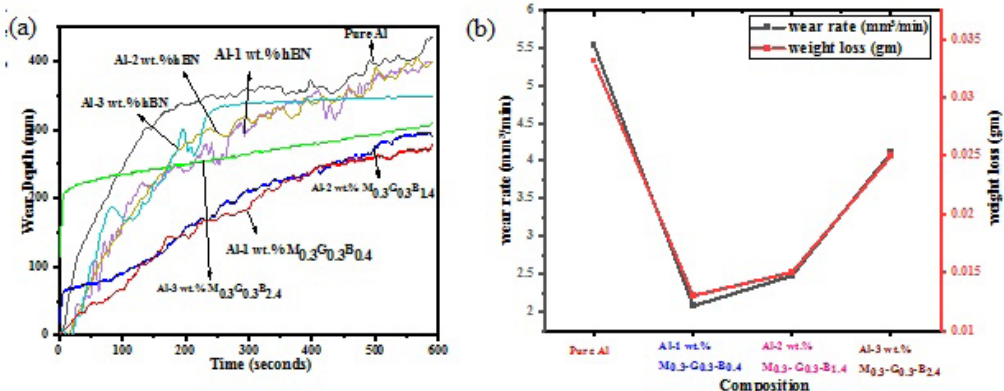


Figure 33. (a) Variation of wear depth of Al-1, 2, 3 wt.% hBN and Al-1, 2 and 3 wt.% CNT-GnP-hBN nanocomposites (b) Wear rate of Al-1, 2 and 3 wt.% CNT-GnP-hBN nanocomposites.

However, it should be noted that both the relative densities and the hardness were found to be lower when the ternary hybrid nanofiller was added to the Al matrix as compared to the hBN monofiller (Figure 31 and Figure 32). Thus, it can be concluded that although the hBN monofiller resulted in better densification and hardness it did not provide poorer wear resistance than the CNT-GnP-hBN ternary hybrid nanofiller. It should be noted that the addition of 1 wt.% of CNT_{0.3}GnP_{0.3}hBN_{0.4} hybrid nanofiller also resulted in the highest hardness as well as relative density among all the Al-CNT-GnP-hBN nanocomposites. The hybrid reinforcement provided a major improvement in the tribological properties of the nanocomposites because of its self-lubricating properties. The addition of the hybrid nanofiller higher than 1 wt.% in the Al matrix deteriorates the wear resistance of the nanocomposite. Material removal was also increased in the case of 2 and 3 wt.% loading level of reinforcement (Figure 33b). The variation of wear depth with time was irregular and shows unexpected jumps, indicating nonuniform densification of the samples. There is a sudden increase in the wear depth within the initial few seconds of the wear test, as the outer layer of the samples were poorly sintered and easily worn out during the wear test. Most of the nanocomposites (Al-2, 3 wt.% CNT-GnP-hBN) showed a continuous increase in the wear depth with time. However, in the case of Al-1 wt.% CNT-GnP-hBN nanocomposite the wear depth reached a steady state after some period of the wear test^{68,69}. It should be noted that all the Al-based nanocomposites showed better wear resistance than the pure Al sample developed similarly.

There is a significant effect of the addition of carbonaceous nanofillers like CNT and GnP on the wear resistance of the Al-based hybrid nanocomposites. hBN when added alone to the Al matrix, is not very effective in improving the wear resistance of Al. The best wear resistance was seen in the case of Al-1 wt.% CNT_{0.3}GnP_{0.3}hBN_{0.4} nanocomposite. The tribological properties and the wear mechanism was determined from the SEM images of the wear tracks in Figure 34. The CNT_{0.3}GnP_{0.3}hBN_{0.4} was found to be the optimum composition of the ternary hybrid nanofiller which gave the best wear resistance among all the Al-CNT-GnP-hBN nanocomposites. An increase in the loading level of the hBN in the ternary hybrid nanofiller deteriorated the wear resistance of the Al-based nanocomposite due to the agglomeration of the

nanofiller at the Al grain boundaries²⁰. Figure 34a, 34f show deep ploughing and delamination in the wear track of the pure Al sample. The width of the wear track of the pure Al sample was ~1.48 mm whereas the width of the wear track of Al-1 wt.% CNT_{0.3}GnP_{0.3}hBN_{0.4} nanocomposite was ~429.28 μm. The width of the Al-3 wt.% hBN nanocomposite showing the best wear resistance among all the Al-hBN nanocomposites was ~1.19 mm. The SEM images of the wear track of Al-1 wt.% CNT_{0.3}GnP_{0.3}hBN_{0.4} nanocomposite in Figure 34c, 34h show a lesser extent of ploughing and a considerably lower width of the wear track. This is because 0.3 wt.% of GnP and 0.4 wt.% of hBN nanofiller gives a highly effective lubricating property which reduces the friction between the steel ball and the matrix surface, whereas 0.3 wt.% of MWCNT in the ternary hybrid nanofiller improved the fracture toughness of the matrix and protects Al particles from being pulled out during the wear test. The 1D CNTs provided an anchoring effect, whereas the 2D GnP and hBN provided wear resistance by forming a lubricating film on the wear track. The SEM images in Figure 34e, 34j of Al-1 wt.% CNT_{0.3}GnP_{0.3}hBN_{2.4} nanocomposite shows that as the loading level of the hBN nanofiller is increased from 0.4 to 2.4 wt.% and fixing MWCNT and GnP wt.% to 0.3 respectively, the width of wear increased from ~429.28 μm to ~845.88 μm. The extent of ploughing and delamination increases as the loading level of reinforcement is increased. Figure 35a shows the dry sliding wear test of the Al-CNT-GnP-hBN nanocomposite. It shows the forces acting at the point of contact of the indenter with the sample. Shear force applied during the wear test could also cause further exfoliation of the 2D nanofillers. The load applied to the indenter could apply a tangential shear force on the 2D nanofillers which could lead to further exfoliation of GnP and hBN and removal from the wear track. 2D materials are expected to be more visible in the wear debris, whereas MWCNTs due to their high aspect ratio are expected to be embedded in the Al matrix and prevent the Al matrix from being pulled out during the wear test. Figure 35b is a schematic diagram showing the abrasive wear mechanism⁷⁰.

Figure 36a shows the XRD spectra of the wear debris collected from the wear track of Al-1 wt.% CNT_{0.3}GnP_{0.3}hBN_{0.4} and Al-3 wt.% CNT_{0.3}GnP_{0.3}hBN_{2.4} nanocomposites. The XRD spectra of the wear debris show peaks mainly corresponding to the various diffraction planes of FCC Al.

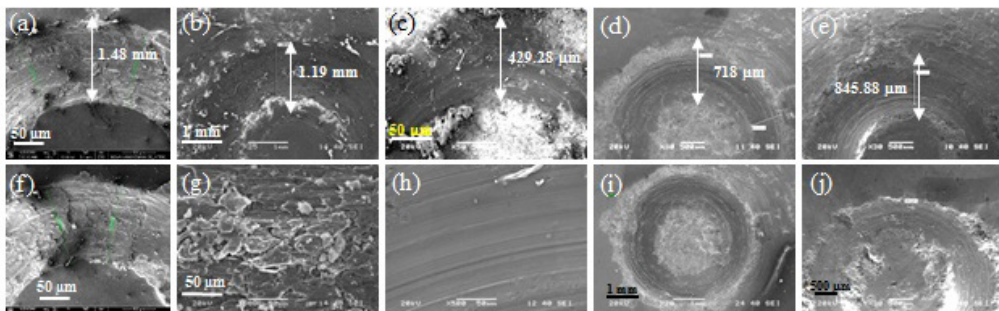


Figure 34. SEM images of the wear tracks of (a, f) pure Al (b, g) Al-3 wt.% hBN (c, h) Al-1 wt.% CNT-GnP-hBN (d, i) Al-2 wt.% CNT-GnP-hBN (e, j) Al-3 wt.% CNT-GnP-hBN nanocomposites.

The (002) peak of CNT, GnP, and hBN which are very close to each other was seen at 2θ value of $\sim 31.03^\circ$ and is very faint and cannot be detected due to the trace amount of the hybrid nanofiller in the wear debris. The intensity of the (002) peak of the hybrid nanofiller was very faint as compared to the sharp high-intensity peaks of Al. This clearly suggests that mainly the Al particles

are pulled out from the wear track during the wear test whereas the hybrid nanofiller remains adhered to the wear track. Figure 37 shows the SEM image of the wear debris of Al-3 wt. % CNT_{0.3}GnP_{0.3}hBN_{2.4} nanocomposite along with elemental maps of B, N, O, and C clearly indicating both Al particles and the ternary hybrid nanofiller in the wear debris.

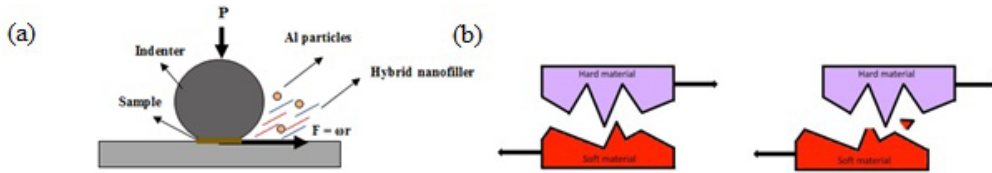


Figure 35. (a) Dry sliding wear test (b) Abrasive wear mechanism.

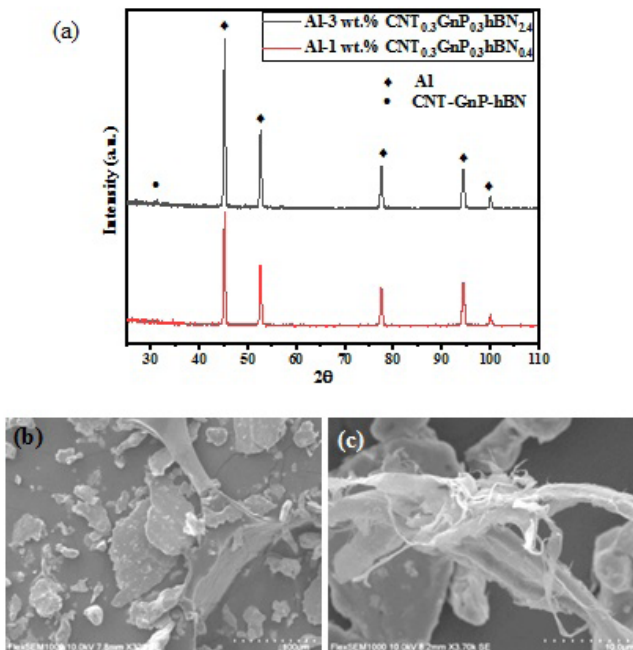


Figure 36. (a) XRD Al-1 wt. % CNT_{0.3}GnP_{0.3}hBN_{2.4} and Al-3 wt. % CNT_{0.3}GnP_{0.3}hBN_{2.4} nanocomposites and SEM image of wear debris of (b) Al-1 wt. % CNT_{0.3}GnP_{0.3}hBN_{2.4} and (c) Al-3 wt. % CNT_{0.3}GnP_{0.3}hBN_{2.4} nanocomposites.

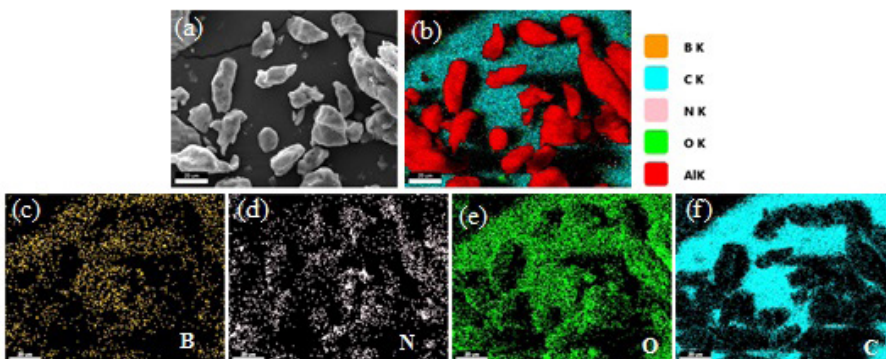


Figure 37. (a) SEM image and (b) Combined elemental map of wear debris of Al-3 wt. % CNT_{0.3}GnP_{0.3}hBN_{2.4} nanocomposite. Elemental map of (c) B (d) N (e) O and (f) C.

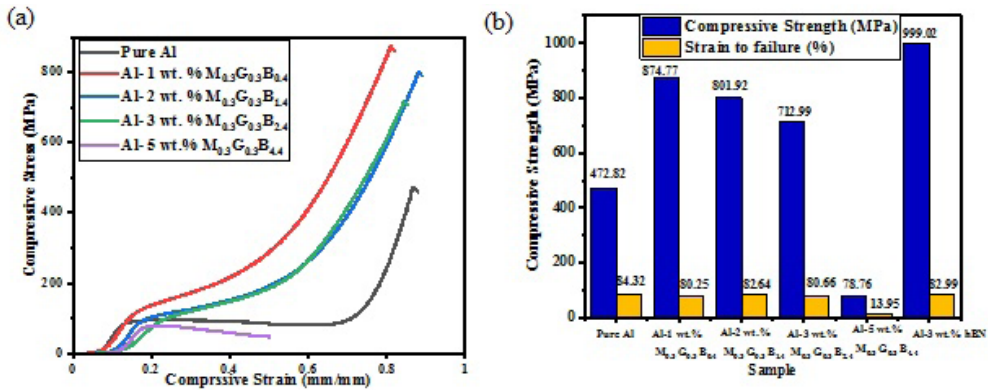


Figure 38. (a) σ - ϵ plots (b) σ_{\max} and ϵ_f of sintered pure Al, Al-CNT-GnP-hBN and Al-hBN nanocomposites.

Figure 38a shows the σ - ϵ plot obtained from the compressive tests of the various Al-CNT-GnP-hBN nanocomposites. Al-1 wt.% CNT_{0.3}GnP_{0.3}hBN_{0.4} nanocomposite shows the highest value of the maximum compressive strength (σ_{\max}) of ~874.77 MPa (Figure 38b) and showed an increase of ~85.01% with respect to the pure Al sample developed similarly which had a σ_{\max} value of ~472.82 MPa. Beyond the addition of 1 wt.% of the ternary hybrid nanofiller the compressive strength of the nanocomposite decreases with the increase in the loading level of the hybrid nanofiller (Figure 38b). This is due to the agglomeration and nonhomogeneous distribution of the nanoreinforcement in the Al matrix at a higher loading level of the ternary hybrid nanofiller which adversely affects the densification of the nanocomposites increasing the porosity in them and resulting in lower relative density. Uniform distribution of the nanoreinforcement in the nanocomposites is a highly effective method to achieve strengthening in the nanocomposites. Nanoparticles distributed homogeneously in the matrix act as a barrier to the dislocation motion thus enhancing the mechanical properties of the nanocomposite^{71,72}. It should be noted that Al-5 wt.% CNT_{0.3}GnP_{0.3}hBN_{4.4} nanocomposite showed the lowest ductility having a strain to failure (ϵ_f) of ~13.95% whereas the ϵ_f value of the Al-1 wt.% CNT_{0.3}GnP_{0.3}hBN_{0.4} nanocomposite was found to be the highest (~80.25%) among all the Al-CNT-GnP-hBN nanocomposites. With the increase in the loading level of the CNT-GnP-hBN ternary hybrid nanofiller both the compressive strength as well as ductility decreases. It should be noted that the Al-3 wt.% hBN nanocomposite showed the highest compressive strength (σ_{\max}) of 999.02 MPa.

4. Conclusions

In the present study three different nanofillers CNT, GnP and hBN have been combined in the form of a ternary hybrid nanofiller and added to the Al matrix to develop Al-based hybrid nanocomposites. The following conclusions could be drawn from the present work.

1. Highly crystalline graphite nanoplatelets (GnP) having few layers of graphene stacked together could be synthesized by the thermal exfoliation of the graphite intercalation compound (GIC) followed by ultrasonication for 20 h in acetone. The GnP had very low defect density.

2. hBN nanoplatelets having very few layers of hBN stacked together were successfully synthesized from the as-received bulk hBN by milling in wet medium. Although the exfoliation of hBN was found to be more difficult than that of natural flake graphite (NFG). TEM analysis has proven that the ball milling was highly effective in exfoliating bulk hBN.
3. The CNT-GnP-hBN ternary nanofiller was found to be highly effective in improving the wear resistance of the Al-based hybrid nanocomposites as compared to the hBN monofiller. The Al-1 wt.% GnP_{0.3}MWCNT_{0.3}hBN_{0.4} hybrid nanocomposite showed the lowest wear depth of the wear track and has the lowest width of the wear track. It also showed the lowest wear rate. Al-3 wt.% hBN nanocomposite showed the best wear properties among the Al-hBN nanocomposites. However, it was much lower than that of Al-1 wt.% CNT_{0.3}GnP_{0.3}hBN_{0.4} hybrid nanocomposite. The ternary CNT-GnP-hBN hybrid nanofiller was found to be more effective than the hBN monofiller in improving the wear resistance of the nanocomposite. However, the hBN monofiller was found to enhance the relative density and hardness of the nanocomposites more effectively than the CNT-GnP-hBN hybrid nanofiller.
4. An increase in the loading level of the hBN in the CNT-GnP-hBN ternary nanofiller beyond 0.4 wt.% deteriorated the physical, mechanical as well as the wear properties of the Al-based nanocomposites. The Al-2 wt.% CNT_{0.3}GnP_{0.3}hBN_{1.4}, Al-3 wt.% CNT_{0.3}GnP_{0.3}hBN_{2.4}, and Al-5 wt.% CNT_{0.3}GnP_{0.3}hBN_{4.4} hybrid nanocomposites all showed a deterioration of relative density, hardness, wear resistance and compressive strength as compared to the Al-1 wt.% CNT_{0.3}GnP_{0.3}hBN_{0.4} hybrid nanocomposite. An increase in the loading level of the hBN in the hybrid nanofiller deteriorated the relative density, hardness, wear properties and compressive strength of the nanocomposites due to the agglomeration of the hybrid nanofiller at the Al grain boundaries.

- Among the Al-CNT-GnP-hBN nanocomposites Al-1 wt.% CNT_{0.3}GnP_{0.3}hBN_{0.4} hybrid nanocomposite was found to show the highest relative density of ~92.56% and highest hardness of ~415.91 MPa. The hardness of Al-1 wt.% CNT_{0.3}GnP_{0.3}hBN_{0.4} nanocomposite was also found to be higher (~22.62%) than the hardness of the sintered pure Al sample developed similarly. The Al-1 wt.% CNT_{0.3}GnP_{0.3}hBN_{0.4} nanocomposite having lower wt.% of hBN showed the highest relative density and the relative density decreases with the increase in hBN content to 4.4 wt.% in the hybrid nanofiller.
- The highest compressive strength (σ_{\max}) of ~ 874.77 MPa was found in the case of Al-1 wt.% CNT_{0.3}GnP_{0.3}hBN_{0.4} hybrid nanocomposite. Beyond the addition of 1 wt.% of the CNT-GnP-hBN nanofiller there was a gradual decrease in the compressive strength of the Al-CNT-GnP-hBN nanocomposites. The sintered pure Al sample developed similarly showed a σ_{\max} value of ~ 472.82 MPa whereas Al-5 wt.% CNT_{0.3}GnP_{0.3}hBN_{4.4} nanocomposite showed a σ_{\max} value of ~78.76 MPa. The Al-1 wt.% CNT_{0.3}GnP_{0.3}hBN_{0.4} hybrid nanocomposite also showed the highest ductility with an ϵ_f value of ~80.25% whereas Al-5 wt.% CNT_{0.3}GnP_{0.3}hBN_{4.4} nanocomposite showed the lowest ductility with ϵ_f value of ~13.95%. The ϵ_f value of the sintered pure Al sample was ~84.32%.
- Majety S, Cao XK, Dahal R, Pantha BN, Li J, Lin JY et al. Semiconducting hexagonal boron nitride for deep ultraviolet photonics. *Quantum Sensing and Nanophotonic Devices IX*; 2012 Jan 21-26; San Francisco, United States. Bellingham: SPIE Digital Library; 2012. p. 82682R.
- Wang L, Bai Y, Ma Z, Ge C, Guan H, Zhang XD. Tribological performances of hexagonal boron nitride nanosheets via surface modification with silane coupling agent. *SN Applied Sciences*. 2021;3:368.
- Park HJ, Cha J, Choi M, Kim JH, Tay RY, Teo EHT et al. One-dimensional hexagonal boron nitride conducting channel. *Sci Adv*. 2020;6(10):eaay4958.
- Tang YB, Lee CS, Chen ZH, Yuan GSD, Kang ZH, Luo LB et al. High-quality graphenes via a facile quenching method for field-effect transistors. *Nano Lett*. 2009;9(4):1374-7.
- Partoens B, Peeters FM. From graphene to graphite: electronic structure around the K point. *Phys Rev B Condens Matter Mater Phys*. 2006;74(7):075404.
- Lee C, Wei X, Kysar JW, Hone J. Measurement of the elastic properties and intrinsic strength of monolayer graphene. *Science*. 2008;321(5887):385-8.
- Bhattacharya A, Bhattacharya S, Das GP. Band gap engineering by functionalization of BN sheet. *Phys Rev B Condens Matter Mater Phys*. 2012;85(3):035415.
- Falin A, Cai Q, Santos EJJ, Scullion D, Qian D, Zhang R et al. Mechanical properties of atomically thin boron nitride and the role of interlayer interactions. *Nat Commun*. 2017;8:15815.
- Ma J, Luo N, Xie Z, Chen F, Fu Q. Preparation of modified hexagonal boron nitride by ball-milling and enhanced thermal conductivity of epoxy resin. *Mater Res Express*. 2019;6(10):1050d8.
- Shaikh MBN, Arif S, Aziz T, Waseem A, Shaikh MAN, Ali M. Microstructural, mechanical and tribological behaviour of powder metallurgy processed SiC and RHA reinforced Al-based composites. *Surf Interfaces*. 2019;15:166-79.
- Aabid A, Murtuza MA, Khan SA, Baig M. Optimization of dry sliding wear behavior of aluminium-based hybrid MMC's using experimental and DOE methods. *J Mater Res Technol*. 2022;16:743-63.
- Shaikh MBN, Arif S, Siddiqui MA. Fabrication and characterization of aluminium hybrid composites reinforced with fly ash and silicon carbide through powder metallurgy. *Mater Res Express*. 2018;5(4):046506.
- Awotunde MA, Adegbenjo AO, Obadele BA, Okoro M, Shongwe BM, Olubambi PA. Influence of sintering methods on the mechanical properties of aluminium nanocomposites reinforced with carbonaceous compounds: a review. *J Mater Res Technol*. 2019;8(2):2432-49.
- Suthar J, Patel KM. Processing issues, machining, and applications of aluminum metal matrix composites. *Mater Manuf Process*. 2018;33(5):499-527.
- Shaikh MBN, Aziz T, Arif S, Ansari AH, Karagiannidis PG, Uddin M. Effect of sintering techniques on microstructural, mechanical and tribological properties of Al-SiC composites. *Surf Interfaces*. 2020;20:100598.
- Liu J, Khan U, Coleman J, Fernandez B, Rodriguez P, Naher S et al. Graphene oxide and graphene nanosheet reinforced aluminium matrix composites: powder synthesis and prepared composite characteristics. *Mater Des*. 2016;94:87-94.
- Shaikh MBN, Raja S, Ahmed M, Zubair M, Khan A, Ali M. Rice husk ash reinforced aluminium matrix composites: fabrication, characterization, statistical analysis and artificial neural network modelling. *Mater Res Express*. 2019;6(5):056518.
- Khaliq A, Rhamdhani MA, Brooks GA, Grandfield J. Analysis of boron treatment for V removal using AlB₂ and AlB₁₂ based master alloys. In: Grandfield J, editor. *Light metals 2014*. Cham: Springer; 2016. p. 963-8.
- Chen CC, Chen CY, Yang HW, Kuo YK, Lin JS. Phase equilibrium in carbothermal reduction Al₂O₃→AlN studied by thermodynamic calculations. *Atlas J Mater Sci*. 2014;1(2):30-7.

5. Acknowledgements

The authors are grateful for the support provided by SEM Laboratory of the Metallurgical and Materials Engineering Department, FESEM Laboratory of the Ceramic Engineering Department, HRTEM Laboratory of the Chemical Engineering Department, XRD Laboratory and Raman Spectroscopy Laboratory of the Physics and Astronomy Department, UV-Vis Spectroscopy Laboratory of Chemistry Department of NIT Rourkela. We would also like to acknowledge the support provided by HRTEM and DSC/TGA Laboratories at PSG Institute of Advanced Studies, Coimbatore, India in analyzing our samples.

6. References

- Telang AK, Rehman A, Dixit G, Das S. Iternate materials in automobile brake disc applications with emphasis on Al composites - a technical review. *J Eng Res Stud*. 2010;1(1):35-46.
- Smith CA. Discontinuous reinforcements for metal matrix composites. In: Miracle DB, Donaldson SL, editors. *ASM handbook: volume 21 – composites*. Materials Park: ASM International; 2001. p. 51-5.
- Fatchurrohman KJN, Iskandar I, Suraya S. Sustainable analysis in the product development of Al-Metal Matrix composites automotive component. *Appl Mech Mater*. 2015;695:32-5.
- Peigney A, Laurent C, Flahaut E, Besca R, Rousset A. Specific surface area of carbon nanotubes and bundles of carbon nanotubes. *Carbon*. 2001;39(4):507-14.
- Jang SH, Kawashima S, Yin H. Influence of carbon nanotube clustering on mechanical and electrical properties of cement pastes. *Materials*. 2016;9(4):220.

25. Farokhzadeh K, Edrissy A. Surface hardening by gas nitriding. In: Hashmi MSJ, editor. *Comprehensive materials finishing*. Amsterdam: Elsevier; 2017. p. 107-36. (Reference Module in Materials Science and Materials Engineering; 2).
26. Rüdorff W. Graphite intercalation compounds. *Adv Inorg Chem Radiochem*. 1959;1:223-66.
27. Siburian R, Sihotang H, Raja SL, Superno M, Simanjuntak C. New route to synthesize graphene nano sheets. *Orient J Chem*. 2018;34(1):182-7.
28. Wang X, Zhang L. Green and facile production of high-quality graphene from graphite by the combination of hydroxyl radicals and electrical exfoliation in different electrolyte systems. *RSC Advances*. 2019;9:3693-703.
29. Stankovich S, Dikin DA, Piner RD, Kohlhaas KA, Kleinhammes A, Jia Y et al. Synthesis of graphene-based nanosheets via chemical reduction of exfoliated graphite oxide. *Carbon*. 2007;45:1558-65.
30. Sinha S, Warner JH. Recent progress in using graphene as an ultrathin transparent support for transmission electron microscopy. *Small Struct*. 2021;2:2000049.
31. Fesneko O, Dovbeshko G, Dementjev A, Karpicz R, Kaplas T, Svirko Y. Graphene enhanced Raman spectroscopy of thymine adsorbed on single-layer graphene. *Nanoscale Res Lett*. 2015;10:163.
32. Ferrarri AC, Meyer JC, Scardaci V, Casiraghi C, Lazzeri M, Mauri F et al. Raman spectrum of graphene and graphene layers. *Phys Rev Lett*. 2006;97:187401.
33. Johra FT, Lee JW, Jung WG. Facile and safe graphene preparation on solution based platform. *J Ind Eng Chem*. 2014;20(5):2883-7.
34. Aqel A, El-Nour KMMA, Ammar RAA, Al-Warthan A. Carbon nanotubes, science and technology part (I) structure, synthesis and characterization. *Arab J Chem*. 2012;5(1):1-23.
35. Arunkumar T, Karthikeyan R, Subramani RR, Viswanathan K, Anish M. Synthesis and characterization of multi-walled carbon nanotubes (MWCNTs). *Int J Ambient Energy*. 2020;41(4):452-6.
36. Kiang CH, Endo M, Ajayan PM, Dresselhaus G, Dresselhaus MS. Size effects in carbon nanotubes. *Phys Rev Lett*. 1998;81:1869-72.
37. Schonfelder R, Aviles F, Knapfer M, Azamar-Barrios JA, Gonzalez-Chia PI, Rummelidb MH. Influence of architecture on the Raman spectra of acid-treated carbon nanostructures. *J Exp Nanosci*. 2014;9(9):931-41.
38. Mohan S, Oluwafemi OS, Songca SP, Rouxel D, Miska P, Lewu FB et al. Completely green synthesis of silver nanoparticle decorated MWCNT and its antibacterial and catalytic properties. *Pure Appl Chem*. 2016;88(1-2):71-81.
39. Stobinski L, Lesiak B, Kover L, Toth J, Biniak S, Trykowski G et al. Multiwalled carbon nanotubes purification and oxidation by nitric acid studied by the FTIR and electron spectroscopy methods. *J Alloys Compd*. 2010;501(1):77-84.
40. Okpalugo TIT, Papakonstantinou P, Murphy H, McLoaughlin J, Brown NMD. High resolution XPS characterization of chemical functionalized MWCNTs and SWCNTs. *Carbon*. 2005;43(1):153-61.
41. Bhimanapati GR, Kozuch D, Robinson JA. Large-scale synthesis and functionalization of hexagonal boron nitride nanosheets. *Nanoscale*. 2014;6:11671-5.
42. Deepika, Li LH, Glushenkov AM, Hait SK, Hodgson P, Chen Y. High-efficient production of boron nitride nanosheets via an optimized ball milling process for lubrication in oil. *Sci Rep*. 2014;4:7288.
43. Shenoy MR, Sakunthala A, Vidhya B, Reddy MV. Visible light sensitive hexagonal boron nitride (hBN) decorated Fe₂O₃ photocatalyst for the degradation of methylene blue. *J Mater Sci Mater Electron*. 2021;32:4766-83.
44. Lafont U, Belle CM, van Zeijl H, van der Zwaag S. Self-healing thermally conductive adhesives. *J Intell Mater Syst Struct*. 2014;25(1):67-74.
45. Stenger I, Schue L, Boukchicha M, Berini B, Plaçais B, Loiseau A et al. Low frequency Raman spectroscopy of few-atomic-layer thick hBN crystals. *2D Mater*. 2017;4(3):031003.
46. Bai Y, Zhang J, Wang Y, Cao Z, An L, Zhang B et al. Ball milling of hexagonal boron nitride microflakes in ammonia fluoride solution gives fluorinated nanosheets that serve as effective water-dispersible lubricant additives. *ACS Appl Nano Mater*. 2019;2(5):3187-95.
47. Kim BJ, Kim JP, Park JS. Effects of Al interlayer coating and thermal treatment on electron emission characteristics of carbon nanotubes deposited by electrophoretic method. *Nano Res Lett*. 2014;9:236.
48. Chill JT, Du Frane WL, Sio CK, King GCS, Soderlind JC, Lu R et al. Transformation of boron nitride from cubic to hexagonal under 1-atm helium. *Diam Rel Mater*. 2020;109:108078.
49. Rastogi PK, Sahoo KR, Thakur P, Sharma R, Bawari S, Podila R et al. Graphene-hBN non-van der Waals vertical heterostructures for four- electron oxygen reduction reaction. *Phys Chem Chem Phys*. 2019;21:3942-53.
50. Kim H, Jeong DY, Jang SG, Lee MW. Synergistic effect of BN for the electrical conductivity of CNT/PAN composite fiber. *J Mech Sci Technol*. 2022;36(6):3103-7.
51. Momeni F, Mehrafrouz B, Montazeri A, Rajabpour A. MD-based design of bilayer graphene-hBN heterostructures: an insight into enhanced thermal support. *Int J Heat Mass Transf*. 2020;150:119282.
52. Kharissova OV, Kharisov BI. Variations of interplanar spacing in carbon nanotubes. *RSC Advances*. 2014;4:30807-15.
53. Wang J, Ma F, Sun M. Graphene, hexagonal boron nitride, and their heterostructures: properties and applications. *RSC Advances*. 2017;7:16801.
54. Jiang L, Fan G, Li Z, Kai X, Zhang D, Chen Z et al. An approach to the uniform dispersion of a high volume fraction of carbon nanotubes in aluminium powder. *Carbon*. 2011;46(6):1965-71.
55. Kostoglou N, Polychronopoulou K, Rebholz C. Thermal and chemical stability of hexagonal boron nitride (h-BN) nanoplatelets. *Vacuum*. 2015;112:42-5.
56. Chou YC, Hsieh TF, Hsieh YC, Lin CP, Shu CM. Comparison of MWCNTs and acidified process by HNO₃ on thermal stability by DSC and TG-FTIR. *J Therm Anal Calorim*. 2010;102:641-6.
57. Yilmaz Z, Ay N. Production parameters affecting the synthesis and properties of hBN-SiC composites. *J Aust Ceramic Soc*. 2020;56:99-108.
58. Smeltzer WW. Oxidation of aluminum in the temperature range 400-600°C. *J Electrochem Soc*. 1956;103(4):209.
59. Field DJ. Oxidation of aluminium and its alloys. In: Vasudevan AK, Doherty RD, editors. *Treatise on materials science and technology*. Amsterdam: Elsevier; 1989. p. 523-37. (Aluminum Alloys—Contemporary Research and Applications; 31).
60. Cullity BD, Stock SR. *Elements of X-ray diffraction*. New York: Prentice-Hall; 2001.
61. Paul T, Zhang C, Denis N, Boesl B, Agarwal A. Role of ultrasonic treatment on microstructure, mechanical and tribological behavior of 2D boron nitride reinforced aluminium composites. *Mater Sci Eng A*. 2021;809:140970.
62. Ferguson B, Jaber FS, Kim CS, Rohatgi PK, Cho K. On the strength and strain to failure in particle-reinforced magnesium metal-matrix nanocomposites (Mg MMNCs). *Mater Sci Eng A*. 2012;558:193-204.
63. Zhang Z, Chen DL. Consideration of Orwan strengthening effect in particulate-reinforced metal matrix nanocomposites: a model for predicting their yield strength. *Scr Mater*. 2006;54:1321-6.
64. Ferreira JLANG, Rocha MCG. Tensile properties of polypropylene composites reinforced with alumina nanoparticles and short carbon fibers. *Mater Res*. 2023;26(Suppl 1):e20230041.
65. Rao V, Periyaswamy P, Bejashin ABH, Naveen E, Ramanan N, Teklemariam A. Wear behavioural study of hexagonal boron nitride and cubic boron nitride-reinforced aluminum MMC with sample analysis. *J Nanomater*. 2022;2022:7816372.
66. Senel MC, Gurbuz M, Koc E. Fabrication and characterization of synergistic Al-SiC-GNPs hybrid composites. *Compos Part B Eng*. 2018;154:1-9.

67. Du L, Zhnag W, Liu W, Zhang J. Preparation and characterization of plasma sprayed Ni_3Al -hBNn composite coating. *Surf Coat Tech.* 2010;205(7):2419-24.
68. Ulus H, Üstün T, Eskizeybek V, Şahin ÖS, Avcı A, Ekrem M. Boron nitride-MWCNT/epoxy hybrid nanocomposites: preparation and mechanical properties. *Appl Surf Sci.* 2014;318:37-42.
69. Gopinath S, Prince M, Raghav GR. Enhancing the mechanical, wear and corrosion behaviour of stir casted aluminium 6061 hybrid composites through the incorporation of boron nitride and aluminium oxide particles. *Mater Res Express.* 2020;7(1):016582.
70. Sahoo S, Samal S, Bhoi B. Fabrication and characterization of novel Al-SiC-hBN self lubricating hybrid composites. *Mater Today Commun.* 2020;25:101402.
71. Gostariani R, Ebrahimi E, Asadabad MA, Paydar MH. Mechanical properties of Al/BN nanocomposites fabricated by planetary ball milling and conventional hot extrusion. *Acta Metall Sin Engl Lett.* 2018;31(3):245-53.
72. Firestein KL, Steinman AE, Golovin IS, Cifre J, Obratzsova EA, Matveev AT et al. Fabrication, characterization and mechanical properties of spark plasma sintered Al-BN nanoparticle composites. *Mater Sci Eng A.* 2015;642:104-12.